

Multiscale model of primary motor cortex circuits reproduces *in vivo* cell type-specific dynamics associated with behavior

Salvador Dura-Bernal^{1,2*}, Samuel A Neymotin², Benjamin A Suter³, Joshua Dacre⁴, Julia Schiemann^{4,5}, Ian Duguid⁴, Gordon MG Shepherd³, William W Lytton^{1,6}

*For correspondence:

salvadord.dura-bernal@downstate.edu (SDB)

¹Department of Physiology and Pharmacology, State University of New York Downstate Health Sciences University, United States; ²Center for Biomedical Imaging and Neuromodulation, Nathan S. Kline Institute for Psychiatric Research, United States; ³Department of Physiology, Northwestern University, United States; ⁴Centre for Discovery Brain Sciences, Edinburgh Medical School: Biomedical Sciences, University of Edinburgh, United Kingdom; ⁵Center for Integrative Physiology and Molecular Medicine, Saarland University, Germany; ⁶Department of Neurology, Kings County Hospital Center, Brooklyn, USA

15

Abstract Understanding cortical function requires studying its multiple scales: molecular, cellular, circuit and behavior. We developed a biophysically detailed multiscale model of mouse primary motor cortex (M1) with over 10,000 neurons, 30 million synapses. Neuron types, densities, spatial distributions, morphologies, biophysics, connectivity and dendritic synapse locations were derived from experimental data. The model includes long-range inputs from thalamic and cortical regions, and noradrenergic inputs from locus coeruleus. Connectivity depended on cell class and cortical depth at sublaminar resolution. The model reproduced and predicted *in vivo* layer- and cell type-specific responses (firing rates and LFP) associated with behavioral states (quiet and movement) and experimental manipulations (noradrenaline receptor blocking and thalamus inactivation), and enabled us to evaluate different hypotheses of the circuitry and mechanisms involved. This quantitative theoretical framework can be used to integrate and interpret M1 experimental data and sheds light on the M1 cell type-specific multiscale dynamics associated with a range of experimental conditions and behaviors.

29

Introduction

Understanding cortical function requires studying its components and interactions at different scales: molecular, cellular, circuit, system and behavior. Biophysically detailed modeling provides a tool to integrate, organize and interpret experimental data at multiple scales and translate isolated knowledge into an understanding of brain function. Previous approaches have emphasized structural aspects based on layers and the broad classification of excitatory and inhibitory neurons (*Potjans and Diesmann, 2014; Douglas et al., 1989*). Modern anatomical, physiological and genetic techniques allow an unprecedented level of detail to be brought to the analysis and understanding of cortical microcircuits (*Luo et al., 2018; Adesnik and Naka, 2018*). In particular, several neuron

39 classes can now be identified based on distinct gene expression, morphology, physiology and connectivity. Cortical excitatory neurons are broadly classified by their axonal projection patterns into 40 intratelencephalic (IT), pyramidal-tract (PT) and corticothalamic (CT) types (*Greig et al., 2013; Harris 41 and Shepherd, 2015; Zeng and Sanes, 2017*). Recent research has also revealed that connections 42 are cell-type and location specific, often with connectivity differences at different cortical depths 43 within layers (*Anderson et al., 2010; Brown and Hestrin, 2009; Morishima and Kawaguchi, 2006*). 44

45 Primary motor cortex (M1) plays a central role in motor control, but has to date only been 46 modeled to a limited extent (*Chadderton et al., 2014; Neymotin et al., 2016b; Heinze et al., 2007; 47 Morishima et al., 2011*). We and others have extensively studied mouse M1 circuits experimentally, 48 and characterized cell subclasses and many cell-type and sublaminar-specific local and long-range 49 circuit connections (*Papale and Hooks, 2017; Shepherd, 2009; Kaneko, 2013*). A major focus of 50 these anatomical and physiological studies has been the distinct cell classes of layer 5 (L5): L5B PT 51 cells – the source of the corticospinal tract, and other pyramidal tract projections, and L5 IT cells 52 which project bilaterally to cortex and striatum. Morphology and physiology differs across the two 53 types. L5 IT cells are thin-tufted and show spike frequency adaptation. L5B PT cells are thick-tufted 54 and show little spike frequency adaptation, but strong sag potentials. In terms of their synaptic 55 interconnectivity these types exhibit a strong asymmetry: connections go from IT to PT cells, but 56 not in the opposite direction (*Kiritani et al., 2012; Morishima and Kawaguchi, 2006*). The strength 57 of their local excitatory input connections is also dependent on PT position within layer 5B, with 58 cells in the upper sublayer receiving the strongest input from layer 2/3 (*Anderson et al., 2010; Hooks 59 et al., 2013; Yu et al., 2008; Weiler et al., 2008*). These and several other highly specific local and 60 long-range wiring patterns are likely to have profound consequences in terms of understanding 61 cortical dynamics, information processing, function and behavior (*Li et al., 2015b*).

62 A key unanswered question in the motor system, and more generally in neural systems (*Mott 63 et al., 2018; Hsu et al., 2020*), is how cell and circuit dynamics relate to behavior. Both IT and PT 64 cell types play a role in motor planning and execution and both have been implicated in motor- 65 related diseases (*Shepherd, 2013*). We have previously shown that the hyperpolarization-activated 66 current (I_h), a target of noradrenergic neuromodulation, is highly expressed in PT cells and affects 67 its synaptic integration and electrophysiological properties (*Sheets et al., 2011*). In vivo studies 68 also reveal noradrenergic neuromodulatory inputs from locus coeruleus (LC) and long-range in- 69 puts from thalamus and cortex causally influence M1 activity and behavioral states (*Boychuk et al., 70 2017; Schiemann et al., 2015; Guo et al., 2021*). Specifically, blocking noradrenergic input to M1 im- 71 paired motor coordination (*Schiemann et al., 2015*), and disrupting the cerebellar-recipient motor 72 thalamus projections to M1 can impair dexterity (*Guo et al., 2021*) or block movement initiation 73 (*Dacre et al., 2021*). These modulatory and long-range projections have been shown to be cell 74 type-specific, and characterized in ex vivo slice experiments (*Sheets et al., 2011; Yamawaki and 75 Shepherd, 2015; Hooks et al., 2013; Suter and Shepherd, 2015*), but how these relate to in vivo activ- 76 ity, including the exact cellular and circuit mechanisms underpinning behavioral state-dependent 77 M1 activity, remain largely unknown. A biologically realistic model of M1 can be used to address 78 this current knowledge gap by generating hypotheses and predictions relating circuit dynamics to 79 function and behavior.

80 We have now developed a multiscale model of mouse M1 incorporating recent experimen- 81 tal data and reproducing in vivo layer- and cell type-specific behavior-dependent responses. The 82 model simulates a cylindric cortical volume with over 10 thousand neurons and 30 million synapses. 83 We attempted, as far as possible, to base parameters on data obtained from a single species, strain 84 and age range, and from our own experimental work. However, these data are necessarily incom- 85 plete, and we have therefore combined additional data from multiple other sources. We focused 86 particularly on the role of L5 excitatory neurons, utilizing detailed models of layer 5 IT and PT 87 neurons with full dendritic morphologies of 700+ compartments based on anatomical cell recon- 88 struction and ionic channel distributions optimized to in vitro experimental measures. The task of 89 integrating experimental data into the model required us to develop several novel methodological

90 techniques for network simulation design, including: 1) specifying connections as a function of nor-
91 malized cortical depth (NCD) – from pia to white matter – instead of by layer designations, with a
92 100-150 μm resolution; 2) identifying and including specific dendritic distributions associated with
93 particular inputs using features extracted from subcellular Channelrhodopsin-2-Assisted Circuit
94 Mapping (sCRACM) studies (*Hooks et al., 2013; Suter and Shepherd, 2015*); and 3) utilizing a high-
95 level declarative modeling tool, NetPyNE, to develop, simulate, optimize, analyze and visualize the
96 model (*Dura-Bernal et al., 2019*).

97 Our M1 model exhibited neuronal firing rates and oscillations that depended on cell class, layer
98 and sublaminar location, and behavioral state, consistent with *in vivo* M1 data. Behavioral changes
99 (quiet vs movement) were modeled by modifying noradrenergic inputs from LC and motor thala-
100 mus inputs. Our cortical model also captured the effects of experimental manipulations, including
101 blocking of NA receptors and motor thalamus inactivation. The model provided different multi-
102 scale mechanistic hypotheses for the observed behavioral deficits, linking noradrenaline blockade
103 to cell type specific changes in I_h and/or potassium conductances and the consequent changes in
104 neuronal firing patterns. The simulations generated experimentally-testable quantitative predic-
105 tions about layer- and cell type-specific responses for the different behavioral states and experi-
106 mental manipulations. They also shed new light on the M1 circuitry and biophysical mechanisms
107 associated with dynamic aspects of behavior-related activity, including physiological oscillations
108 and neuromodulation. We are making our model freely available as a community resource so that
109 others can update and extend it, incorporating new data such as that from the M1 multimodal cell
110 census and atlas recently released by the BRAIN Initiative Cell Census Network (*Network, 2021*).

111 Results

112 Overview of model development and simulations

113 We implemented a biophysically-realistic model of the mouse M1 microcircuit representing a cylin-
114 drical volume of 300 μm diameter (Fig. 1). The model included over 10,000 neurons with 35 million
115 synapses. Cell properties, locations, and local and long-range connectivity were largely derived
116 from a coherent set of experimental data. Available experimental data was particularly detailed
117 for two L5 populations that were the focus of this study: pyramidal tract (PT) corticospinal cells
118 and intratelencephalic (IT) corticostriatal cells. One innovative feature in the network presented
119 here was the inclusion of a Layer 4 for motor cortex, consistent with its recent characterization
120 (*Yamawaki et al., 2015; Bopp et al., 2017; Barbas and García-Cabezas, 2015; Network, 2021*). The
121 model was developed using the NetPyNE (*Dura-Bernal et al., 2019*) modeling tool and the NEURON
122 simulation engine (*Carnevale and Hines, 2006*). Over 20,000 simulations were required to progres-
123 sively construct and improve the model. Simulations required over 8 million high performance
124 computing (HPC) cluster core-hours to arrive at the results shown, primarily during model build-
125 ing. One second of simulation (model) time required approximately 96 core-hours of HPC time.
126 We employed a grid search on underconstrained connectivity parameters – e.g. inhibitory to exci-
127 tatory weights – to identify simulations that produced physiologically realistic firing patterns across
128 populations.

129 As expected from results in other systems, there was no single “right” model that produced
130 these realistic firing patterns but rather a family of models (degenerate parameterization) that
131 were within the parameter ranges identified by experiment (*Golowasch et al., 2002; Prinz and
132 Marder, 2003; Edelman and Gally, 2001*). From these, we selected one *base model*, representing
133 a single parameter set, to illustrate in this paper. This base model was tested for robustness by
134 changing randomization settings to provide a *model set*, with analysis of raw and average data
135 from 25 simulations: 5 random synaptic input seeds \times 5 random connectivity seeds (based on
136 connectivity density). This can be considered analogous to testing multiple trials and subjects in
137 an experimental setup. The full model set showed qualitatively similar results with low variance in
138 bulk measures (population rates, oscillation frequencies) for changes in randomization settings.

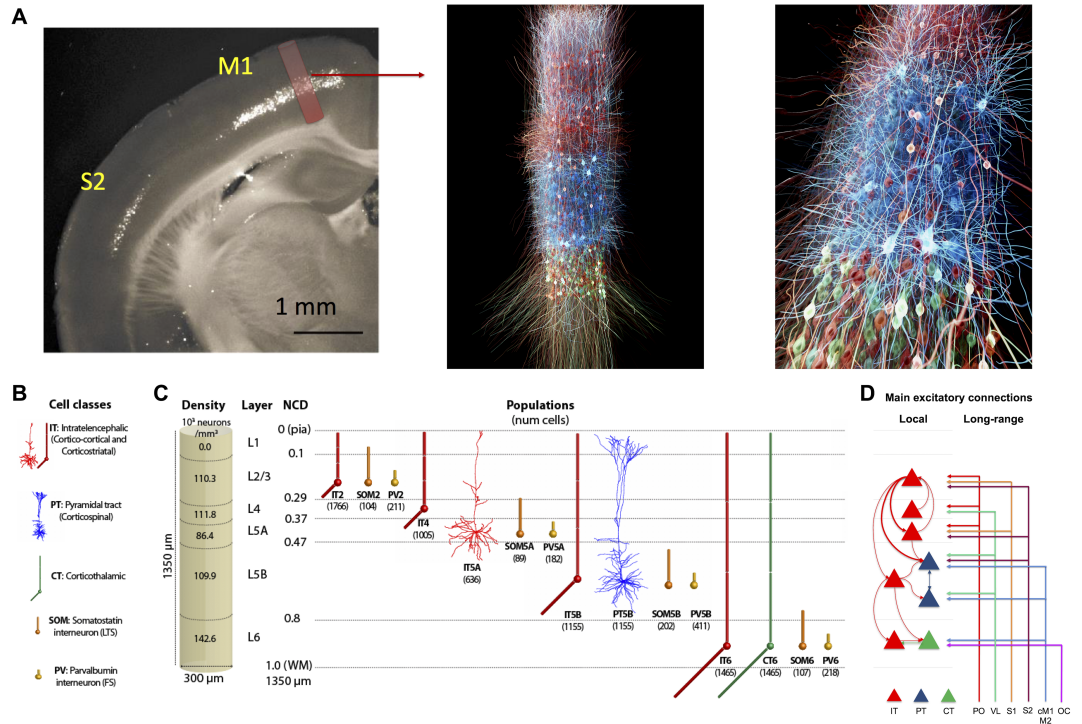


Figure 1. M1 microcircuit model 3D visualization, connectivity, dimensions, and neuronal densities, classes and morphologies. A. (left panel: Epifluorescence image of a coronal brain slice of mouse showing M1 and S1 regions, and approximate anatomical location and volume of simulated cylindrical tissue adapted from (Suter et al., 2013)). middle and right panels 3D visualization of M1 network, showing location and stylized morphologies of 20% of excitatory IT (red), PT (blue) and CT (green) cells, and snapshot of simulated activity with spiking neurons in brighter color (visualization by nicolasantille.com). **B.** Cell classes modeled. IT5A and PT5B neurons are simulated in full morphological reconstructions. Other excitatory types and inhibitory neurons use simplified models with 2-6 compartments. All models are conductance-based with multiple ionic channels tuned to reproduce the cell's electrophysiology. **C.** Dimensions of simulated M1 cylindrical volume with overall cell density per layer designation (left), and cell types and populations simulated (right). **D.** Schematic of main local and long-range excitatory connections (thin line: medium; thick line: strong). Note the unidirectional projections from ITs to PTs, with a particularly strong projection arising from L2/3. (IT: intratelencephalic cells – corticostriatal; PT: pyramidal-tract cells – corticospinal; CT: corticothalamic cells. PO: posterior nucleus of thalamus; VL: ventrolateral thalamus; S1: primary somatosensory; S2: secondary somatosensory; cM1: contralateral M1; M2: secondary motor; OC: orbital cortex; PV: parvalbumin basket cells, SOM: somatostatin interneurons; number of cells in each population shown in brackets; left shows L1–L6 boundaries with normalized cortical depth – NCD from 0 = pia to 1 = white matter.)

139 We used the base model and model set to characterize firing and local field potential (LFP)
140 patterns in response to different levels of long-range inputs and noradrenergic (NA) neuromodula-
141 tion associated with different behavioral states and experimental manipulations of mouse M1
142 *in vivo* (**Schiemann et al., 2015**) (see Table 1). The two behavioral states corresponded to *quiet*
143 wakefulness and self-paced, voluntary *movement*. Each of these states was simulated under three
144 different experimental manipulations: *control*, motor thalamus inactivation (*MTh inactivation*) and
145 blocking input from LC via noradrenergic receptor antagonists (*NA-R block*). The effect of changes
146 in noradrenergic neuromodulation, driven by inputs from locus coeruleus (LC), were simulated
147 by altering I_h conductance in PT cells (see Table 1 and Methods), consistent with *in vitro* findings
148 (**Sheets et al., 2011; Adesnik and Naka, 2018**). Results are presented both in terms of cell class and
149 cell population. We focused on three excitatory classes: intratelencephalic (IT), pyramidal-tract (PT),
150 corticothalamic (CT); and two inhibitory classes: parvalbumin-staining fast-spiking basket cells (PV),
151 somatostatin-staining, low-threshold spiking cells (SOM). Cell populations are defined by both class
152 and by layer (e.g. IT5A indicates class IT in layer 5A; CT6 is class CT in layer 6). We use our results
153 to explain and predict the response of the M1 circuit under the different behavioral states and
154 experimental manipulations simulated.

Experimental manipulation	Behavioral State	MTh input (VL)	NA input (PT I_h)
Control	Quiet	Low (0-2.5 Hz)	Low NA (75% I_h)
Control	Movement	High (0-10 Hz)	High NA (25% I_h)
MTh inactivation	Quiet	Very low (0-0.01 Hz)	Low NA (75 % I_h)
MTh inactivation	Movement	Very low (0-0.1 Hz)	High NA (25% I_h)
NA-R antagonist	Quiet	Low (0-2.5 Hz)	Very low (100% I_h)
NA-R antagonist	Movement	High (0-10 Hz)	Very low (100% I_h)

Table 1. Motor thalamus (MTh) input and noradrenergic (NA) input associated with the different experimental manipulations and behavioral states simulated in the M1 model. NA input is modeled by modifying the conductance of PT I_h .

155 **M1 firing dynamics during quiet wakefulness (spontaneous activity)**

156 We characterized *in vivo* spontaneous activity in the base model. This was simulated based on
157 expected background drive of ≤ 5 Hz from all long-range inputs, and low NA input resulting in
158 medium level I_h (75%) in PT cells (Fig. 2) (**Yamashita et al., 2013; Hirata and Castro-Alamancos,**
159 **2006**). These properties were consistent with the quiet wakefulness state and control conditions
160 as recorded by whole-cell patch-clamp electrophysiology in awake mice *in vivo* (**Schiemann et al.,**
161 **2015**). We validated the M1 model cell type- and layer-specific firing rates against available *in vivo*
162 experimental data from mouse motor cortex (**Schiemann et al., 2015; Zagha et al., 2015; Li et al.,**
163 **2016; Estebanez et al., 2018; Economo et al., 2018**) (Fig. 2B). All population mean and median firing
164 rates ranged between 0.1 and 10 Hz, and maximum rates (excluding outliers) were below 35 Hz, for
165 both model and experiment. More specifically, we compared L2/3 IT (median \pm IQR model=1.8 \pm 4.0
166 Hz, exp=0.3 \pm 0.7 Hz), L5B IT (model=6.5 \pm 8.8 Hz, exp=3.2 \pm 2.5 Hz), L5B PT (model=1.8 \pm 4.8 Hz,
167 exp=4.6 \pm 4.6 Hz). Since certain studies did not distinguish between cell types or sublayers we
168 also compared L5B IT/PT (model=4.8 \pm 8.5 Hz, exp=5.1 \pm 6.0 Hz) and L5 IT/PT (model=5.5 \pm 9.2 Hz,
169 exp1=1.7 \pm 4.0 Hz, exp2=7.6 \pm 8.5 Hz, exp3=2.4 \pm 4.7 Hz). Significant statistical differences among
170 population firing rates from different studies are expected, and therefore these were also expected
171 between model and experiment. An example is L5 IT/PT where two experimental datasets were
172 statistically significantly different (exp1=1.7 \pm 4.0 Hz, exp2=7.6 \pm 8.5 Hz; p = 6.2e-15, rank-sum test),
173 whereas this was not the case when comparing the L5B IT/PT model to experiment (model=5.5 \pm 9.2
174 Hz, exp2=7.6 \pm 8.5 Hz p = 0.43, rank-sum test). Overall, these results indicate that model activity was
175 consistent with *in vivo* mouse data.

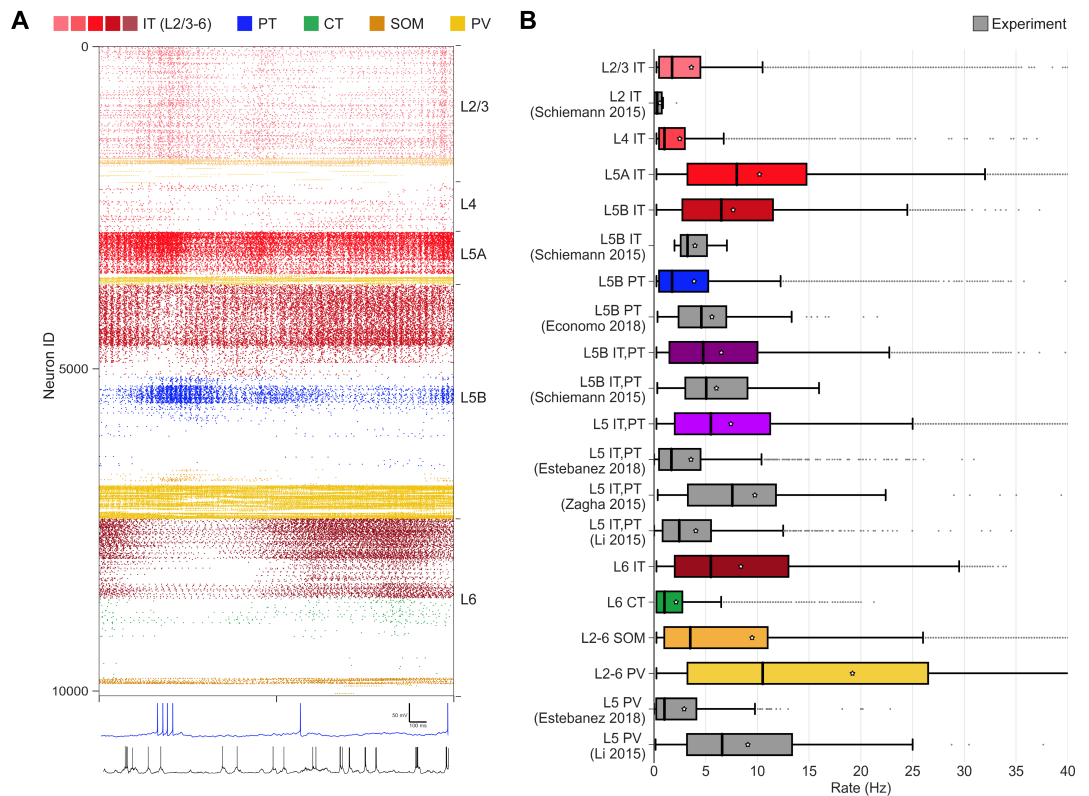


Figure 2. M1 cell type and layer-specific firing dynamics during quiet wakefulness state and control condition (spontaneous activity) The quiet state was simulated by driving the network with background activity (≤ 5 Hz) from all long-range inputs, and medium level I_h (75%) in PT cells (low NA modulation). **A. Top:** Raster plot of mid-simulation activity (2s of base model simulation shown; cells grouped by population and ordered by cortical depth within each population). **Bottom:** Example model (blue) and experiment (black) PT5B voltage traces. **B.** Firing rates statistics (boxplots) for different cell types and layers in the model set (color bars) and experiment (gray bars).

176 Activity patterns were not only dependent on cell class and cortical-layer location, but also sub-
177 laminar location. This supports the importance of identifying connectivity and analyzing activity by
178 normalized cortical depth (NCD) in addition to layer (**Harris and Shepherd, 2015; Anderson et al.,**
179 **2010**). For example, PT cell activity was particularly high superficially in L5B, with firing rates de-
180 creasing with cortical depth (Fig. 2A), consistent with depth-weighted targeting from L2/3 IT pro-
181 jections (**Anderson et al., 2010; Weiler et al., 2008**). This pattern of firing was consistent across
182 network variations with different wiring and input randomization seeds. L5A/B IT exhibited similar
183 cortical-depth dependent activity. L2/3 and L4 IT populations showed overall lower rates than L5
184 IT, consistent with weaker projections onto these populations from local M1 (**Weiler et al., 2008;**
185 **Yamawaki et al., 2015**), and from long-range inputs (**Mao et al., 2011; Suter and Shepherd, 2015; Ya-**
186 **mawaki et al., 2015**). In particular, the main source of L4 IT input was thalamic, in correspondence
187 with the well-described pattern in sensory cortex (**Yamawaki et al., 2015**). Despite the weaker re-
188 sponse, L2/3 IT showed slow oscillatory activity around delta frequency. Within L6, superficial cells
189 of IT and CT populations were more active than deeper ones. This was due to stronger intralam-
190 inar, L5B IT (**Weiler et al., 2008; Yamawaki and Shepherd, 2015**) and long-range inputs, primarily
191 from orbital and contralateral motor cortices (for more details on model connectivity see Methods
192 Fig. 8) (**Hooks et al., 2013**). Weaker local projections onto L6 CT compared to L6 IT resulted in firing
193 rate differences between CT and IT.

194 **M1 firing dynamics during movement**

195 The model reproduced experimental cell type-specific dynamics associated with movement. The
196 movement state was simulated by increasing long-range inputs from ventrolateral thalamus (VL;
197 also called motor thalamus, MTh) to 0-10 Hz (uniform distribution), and reducing I_h conductance to
198 25% in PT cells, to simulate high NA neuromodulatory inputs from LC. The remaining 6 long-range
199 inputs (PO, S1, S2, cm1, M2, OC) continued to provide background drive (< 5Hz). This resulted in
200 a large increase in L5B PT activity and the development of a strong gamma oscillation (Fig. 3A).
201 PT5B_{lower} neurons, which were largely silent during the quiet state, now exhibited similar activity to
202 PT5B_{upper}. This is consistent with the involvement of PT (**Anderson et al., 2010; Peters et al., 2017;**
203 **Kiritani et al., 2012**), and particularly PT5B_{lower} (**Economou et al., 2018**), in motor control. During
204 movement, the activity of L2/3 IT and L5 IT decreased moderately, whereas L4 IT, L6 IT and L6 CT
205 firing rates remained similar. There was a transition period from quiet to movement that lasted
206 approximately 500ms, during which there was a peak in the activity of L5 IT and PT5B_{upper}, consis-
207 tent with VL efferent projections. This transitory activity peaks could also be seen in most of the
208 remaining model set simulations. Although IT2/3 exhibited a similar transition peak in the base
209 model, this was not apparent in other model set simulations, suggesting this could have resulted
210 from the ongoing L2/3 IT delta oscillations.

211 Model firing rate distributions were generally consistent with experimental data across popu-
212 lations and behavioral states. We compared the quiet and movement population firing rates of
213 the model set against M1 *in vivo* experimental data (**Schiemann et al., 2015**) (Fig. 3B). Both model
214 and experiment L2/3 IT cells exhibited low firing rates during both quiet (mean \pm SD model: 1.6 ± 3.9
215 Hz; exp: 0.6 ± 0.7 Hz) and movement states (mean \pm SD model: 0.7 ± 2.8 Hz; exp: 0.6 ± 1.1 Hz). The
216 L5B rates, including both IT and PT, were similar in model and experiment and exhibited a similar
217 increase from quiet (model 4.1 ± 5.5 Hz; exp 5.9 ± 3.9 Hz) to movement (model: 6.9 ± 9.7 Hz; exp:
218 8.4 ± 7.5 Hz). Following the experimental study data analysis (**Schiemann et al., 2015**), we com-
219 pared rates of cells that exhibited enhanced or suppressed activity from quiet to movement. Both
220 L5B_{enhanced} and L5B_{suppressed} rates exhibited comparable trends in model and experiment. The quiet
221 state L5B_{enhanced} mean \pm SD rates were higher in the model than experiment (model: 1.5 ± 3.6 Hz, exp:
222 5.1 ± 4.0 Hz) but increased to a similar rate during movement (model: 13.2 ± 11.1 Hz, exp: 11.3 ± 7.7 Hz).
223 L5B_{suppressed} model and experiment rates exhibited a similar decrease from quiet (model: 7.5 ± 5.7
224 Hz, exp: 5.0 ± 4.2 Hz) to movement states (model: 2.0 ± 3.1 , exp: 2.3 ± 2.7 Hz). L5B IT quiet mean
225 \pm SD rates were higher for model vs experiment (model: 6.7 ± 5.9 Hz, exp: 3.5 ± 2.3 Hz) but also

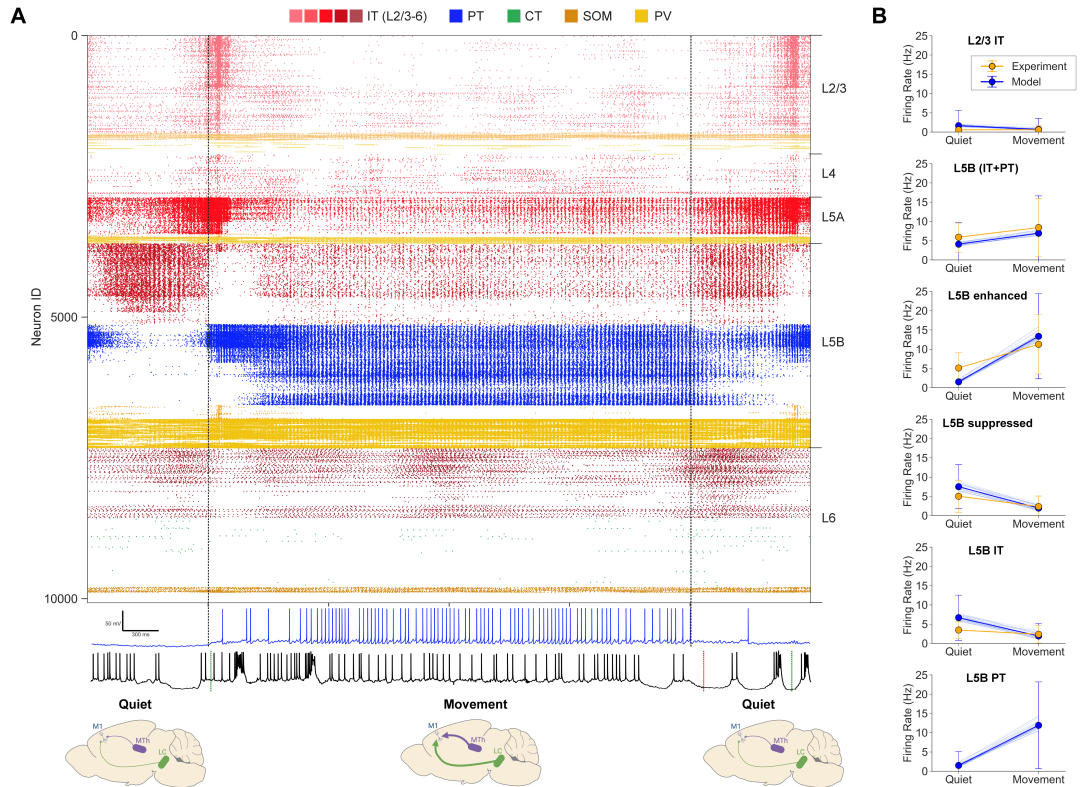


Figure 3. M1 cell-type and layer-specific firing dynamics during the quiet and movement states under the control condition. The movement state was simulated by driving the network with increased activity (0–10Hz) from motor thalamus, background activity (≤ 5 Hz) from the 6 remaining long-range inputs, and reducing I_h to 25% in PT cells (high NA modulation). **A.** Top: Raster plot of activity transitioning from quiet (1s) to movement (4s) to quiet (1s) states (6s of base model simulation shown; cells grouped by population and ordered by cortical depth within each population). Bottom: Example model PT5B (blue) and experiment (black) voltage traces. **B.** Firing rate (mean \pm SD) in different cell populations for model set (blue) and experiment (orange). Model set includes cell rates of all 25 simulations; the mean rates of each individual simulation shown as thin blue lines. Statistics were computed across 4 secs for each state.

decreased to a similar level during movement (model: 1.9 ± 3.3 Hz, exp: 2.4 ± 2.3 Hz). Model L5B PT rates increased sharply from quiet (1.5 ± 3.6 Hz) to movement (11.9 ± 11.3 Hz). We did not include experiment PT rates in Fig. 3B given their small sample size ($N=3$) and high variability. Instead, for reference, we included the L5B rates, which include both IT and PT. However, we note that two of the experiment PT cells showed a decrease from quiet to move (16.0 Hz to 5.6 Hz and 4.7 Hz to 0.6 Hz), and one showed a similar sharp increase to that of the model (3.5 Hz to 13.2 Hz). The robustness of the model was evidenced by the small variability across the mean firing rates of the 25 simulations in the model set, each with different randomization seeds (see thin blue lines in Fig. 3B).

M1 layer 5 LFP oscillations depend on behavioral state

We compared M1 layer 5 LFP signals during quiet and movement states in the model and experimental datasets (Fig. 4). Importantly, the model was not tuned to reproduce the experiment LFP during the quiet or movement states. Despite this, LFP amplitude were similar in model and experiment (order of $500 \mu V$). In both experiment and model, the L5 LFP showed weaker slow oscillations (delta) and stronger fast oscillations (gamma) during movement vs quiet behavioral states. This is illustrated in the raw LFP signal and spectrogram examples for experiment and model (Figure 4A for quiet and 4B for movement). Model L5 LFP was averaged across the signals recorded from simulated extracellular electrodes at 3 depths within L5: 600um (L5A), 800um (upper L5B) and 1000um (lower L5B). The experimental LFP dataset was recorded *in vivo* from L5 extracellular electrodes and preprocessed to remove outliers and potential artifacts (see Methods).

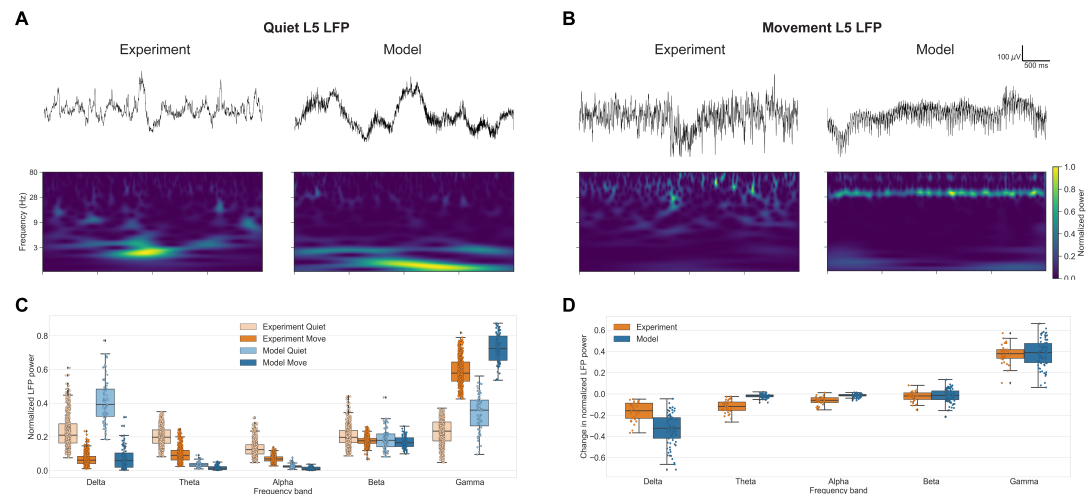


Figure 4. M1 layer 5 LFP oscillations during the quiet and movement states. Example experiment and model raw LFP signals (top) and spectrograms (middle) during the quiet (A) and movement (B) states. C. Comparison of experiment and model normalized power spectral density (PSD) power across 5 frequency bands during quiet and movement states. D. Comparison of experiment and model changes in normalized power spectral density (PSD) power across 5 frequency bands during quiet and movement states .

The model reproduced behavioral-dependent differences across different frequency bands of M1 LFP oscillations. To quantify these differences we calculated the LFP normalized power spectral density (PSD) across the major frequency bands for the experimental and modeling datasets (Fig. 4C). To enable comparison, we segmented the experimental data in 4-second samples, matching the duration of the model dataset samples. Both experiment and model datasets exhibited stronger LFP power at the lower end of the spectrum (delta, theta and alpha bands) during the quiet state, and stronger high-frequency (gamma) LFP power during movement. More specifically, delta (0-4 Hz) power in the quiet state was high in both model vs experiment (median \pm IQR: model: 0.39 ± 0.16 ; exp: 0.21 ± 0.11) but decreased to a similar level during movement (model: 0.06 ± 0.09 ;

255 exp: 0.06 ± -0.04). Theta (4-8 Hz) power was overall higher in experiments compared to the model,
256 but in both cases showed higher amplitude in the quiet vs movement states . A similar pattern
257 was observed for the LFP alpha (8-13 Hz) power (model: 0.02 ± 0.01 vs 0.01 ± 0.02 ; exp: 0.12 ± 0.05
258 vs 0.07 ± 0.03). Beta power (13-30 Hz) remained largely stable from quiet to movement states, and
259 exhibited very similar values for experiment and model (model: 0.18 ± 0.08 and 0.18 ± 0.08 ; exp:
260 0.20 ± 0.07 and 0.18 ± 0.03). Gamma power (30-80 Hz) was stronger during movement for both
261 experiment and model (model: 0.36 ± 0.15 and 0.72 ± 0.14 ; exp: 0.23 ± 0.11 and 0.58 ± 0.11).

262 The model also reproduced the main changes in LFP power from quiet to movement states
263 when looking at paired samples occurring within the same recording. In the previous comparison,
264 the experimental dataset included a larger number of 4-second samples for the quiet (N=3890)
265 than movement (N=2840) states. These were obtained from 30 recordings from different animals,
266 trials and recording sites within L5. In order to more directly quantify the change in LFP power
267 from quiet to movement, we selected the subset of paired 4-second quiet and movement samples
268 that occurred consecutively within the same recording. We then calculated the change in normal-
269 ized LFP PSD for the resulting 160 pairs of consecutive quiet and movement samples (Fig. 4D).
270 Both model and experiment showed results consistent with the previous analysis: from quiet to
271 movement there was 1) a strong decrease of delta frequency power during movement (model:
272 -0.32 ± 0.19 ; exp: -0.16 ± 0.14); 2) small changes in theta, alpha and beta power; and 3) large increase
273 in gamma power (model: 0.39 ± 0.18 ; exp: 0.38 ± 0.08). These results provide further validation that
274 the model is capturing behavior-related oscillatory dynamics observed in mouse M1 in vivo.

275 **M1 dynamics during motor thalamus inactivation**

276 To gain insights into the known role of thalamic inputs in regulating M1 output (*Guo et al., 2021;*
277 *Dacre et al., 2021*) we simulated an experimental manipulation described in our in vivo study (*Schie-*
278 *mann et al., 2015*), consisting of blocking thalamic input by local infusion of the *GABA_A* receptor
279 agonist muscimol into the VL region. Our computational model captured several features of in-
280 activating motor thalamus (MTh) inputs to M1. The MTh inactivation condition was simulated by
281 removing the VL input, thus driving the network with the remaining 6 long-range background in-
282 puts (PO, cM1, M2, S1, S2, OC). Under this condition, the change from quiet to movement states
283 only involved reducing I_h conductance from 75% to 25% in PT cells, simulating high NA neuromod-
284 ulatory inputs from LC. In the model, the major changes under the thalamus inactivation condition
285 were observed during the movement state (Fig. 5A,B): a decrease in overall L5B activity (control:
286 6.9 ± 9.7 Hz, MTh inact: 4.00 ± 5.7 Hz) consistent with experiment (control: 8.4 ± 7.5 Hz, MTh inact:
287 2.2 ± 4.0 Hz). Similarly, the model captured the strong reduction of MTh inactivation in the L5B_{enhanced}
288 population during movement (model control: 13.3 ± 11.1 Hz, MTh inact: 6.3 ± 7.1 Hz; exp control:
289 11.3 ± 7.7 , MTh inact: 4.2 ± 4.9). The decrease in the model L5B rates was caused by a strong reduction
290 of PT rates (control: 11.9 ± 11.3 Hz, MTh inact: 2.9 ± 6.0 Hz). MTh inactivation resulted in a particularly
291 strong reduction of the movement-associated PT5B_{lower} population, which was practically silenced.

292 However, results suggested that the model was not adequately capturing some effects of MTh
293 inactivation on M1 L5B, particularly during the quiet state. Specifically, MTh inactivation lead to
294 a reduction of quiet state L5B (control: 5.1 ± 3.9 Hz, MTh inact: 1.1 ± 1.1), as well as L5B_{suppressed},
295 which was not observed in our model, where these two populations rates remained similar. We
296 hypothesized this could be due to the lack of interaction between long-range inputs in the model,
297 preventing it from capturing the effects of MTh inactivation on other regions (e.g. M2) that in turn
298 provide input to M1 (see Discussion for more details and alternatives). To evaluate this hypothesis
299 we modified our original model of MTh inactivation by reducing the activity of other cortical long-
300 range inputs (cM1, M2). The modified model better reproduced experimental L5B and L5B_{suppressed}
301 results, including those during the quiet state (see Fig. 5B purple lines), supporting our hypothesis
302 of the circuitry involved in the MTh inactivation condition.

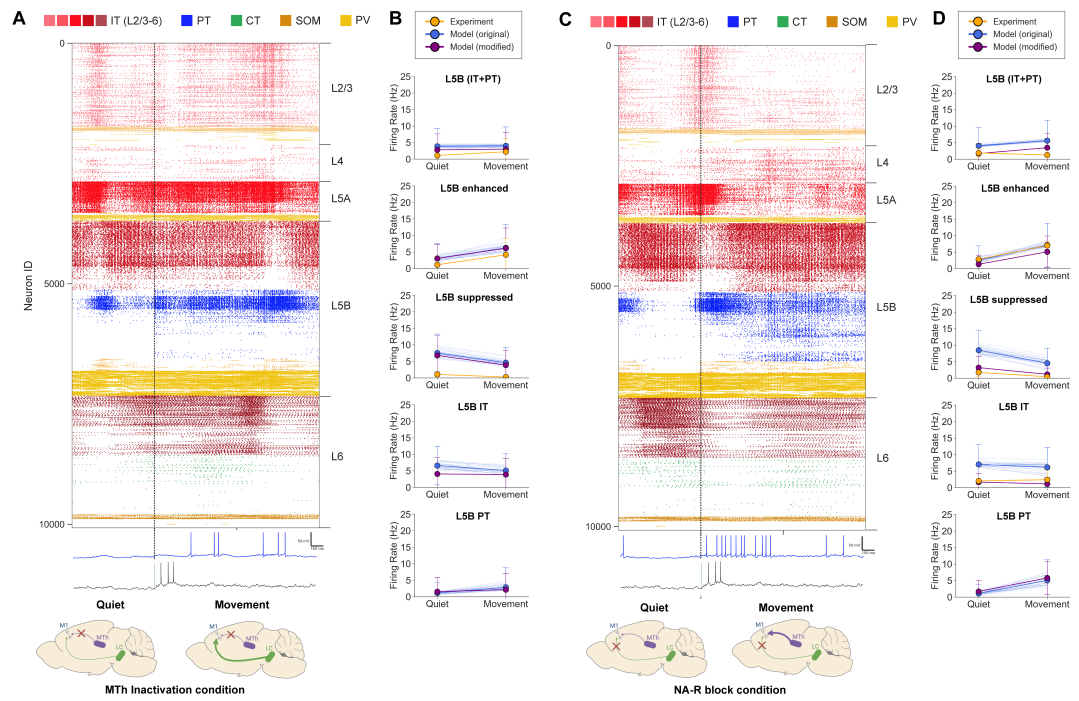


Figure 5. M1 cell-type and layer-specific firing dynamics during the quiet and movement states for the MTh inactivation (A and B) and the NA-R block (C and D) conditions. A. and C. Top: Raster plot of activity transitioning from quiet (1s) to movement (2s) (3s of base model simulation shown; cells grouped by population and ordered by cortical depth within each population). **Bottom:** Example model PT5B (blue) and experiment (black) voltage traces. **B. and D.** Firing rate (mean \pm SD) in different cell populations for the original model set (blue), modified model (purple) and experiment (orange). The modified model decreased long-range inputs from cM1 and M2 for the MTh inactivation condition, and increased K⁺ conductance for the NA-R block condition. The original model set includes cell rates of all 25 simulations; the mean rates of each individual simulation shown as thin blue lines. Statistics were computed across 4 secs for each state.

303 **M1 dynamics during noradrenergic (NA) receptor blockade**

304 We then explored the role of NA neuromodulation, which has been shown to influence M1 activity
305 during movement (*Dacre et al., 2021; Guo et al., 2021; Sheets et al., 2011*), by simulating the dis-
306ruption of NA signaling in M1 through local infusion of NA-R antagonists (*Schiemann et al., 2015*).
307 The model reproduced key aspects of the experimental M1 L5B responses under the noradrener-
308gic receptor blocking (NA-R block) condition. The NA-R block condition was initially simulated by
309fixing the I_h conductance in PT cells to 100%, reflecting the lack of NA modulation from LC. The
310long-range inputs from seven cortical and thalamic regions were kept the same as in the control
311condition. Under this condition, the change from quiet to movement states only involved increas-
312ing the firing rate of inputs from VL (MTh). NA-R block resulted in decreased L5B activation
313during movement compared to control condition (Fig. 5C,D) (control: 6.9 ± 9.7 Hz, NA-R block: 5.6 ± 6.2
314Hz), particularly in the PT5B population (control: 11.9 ± 11.3 Hz Hz, NA-R block: 5.1 ± 6.3 Hz). In vivo
315experiments also showed a decrease in L5B movement rates, although this was more pronounced
316(control: 8.4 ± 7.5 Hz, NA-R block: 1.3 ± 2.2 Hz). A similar decrease during NA-R block was observed
317in the quiet rates of L5B and L5B IT, whereas these model populations remained at a similar rate
318than in the control condition.

319 These results suggested, as in the MTh inactivation condition, that the model was not fully
320capturing some effects of LC inputs. We therefore modified our model to incorporate an additional
321known effect of NA, namely, the modulation of potassium (K^+) conductance (*Sheets et al., 2011;*
322*Wang and McCormick, 1993; Favero et al., 2012; Schiemann et al., 2015*). Increased NA has been
323shown to reduce K^+ conductance, hence to simulate this effect during the NA-block condition
324we increased potassium conductance by 50 % in all excitatory cell types. The combined effect of
325increasing I_h and K^+ better captured the experimental responses during the NA-block condition
326(see Fig. 5D purple lines). More specifically, L5B, L5 IT and L5B_{suppressed} mean firing rates were lower
327for both the quiet and move responses, closely matching those recorded *in vivo*. This supports
328the hypothesis that changes in K^+ conductance are an important component of LC-mediated NA
329modulation.

330 **Motor thalamic and noradrenergic inputs affect L5B dynamics in a cell type and**
331 **sublayer-specific manner**

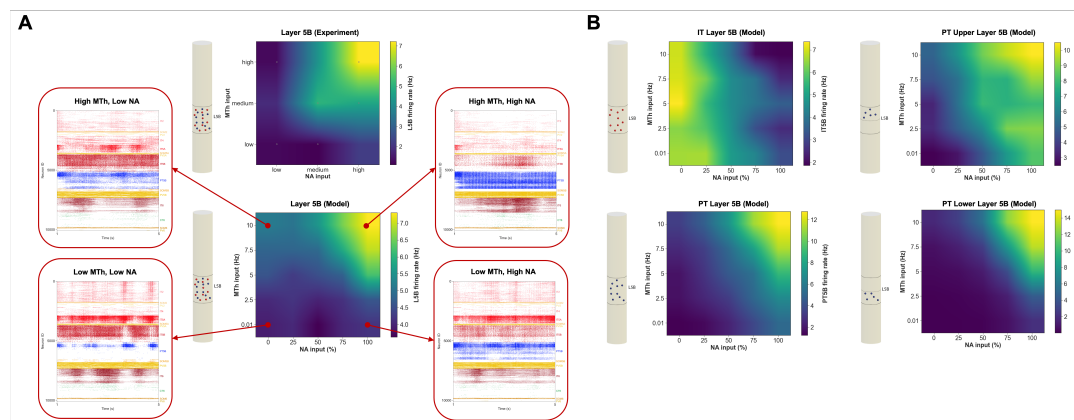


Figure 6. Cell type and sublayer-specific effects of MTh and NA input levels on L5B dynamics **A.** Mean L5B firing rate response of experiment (top) and model (bottom) to different levels of MTh and NA inputs. Firing raster plot of full circuit model shown inset for each of the four extreme conditions. Schematic cylinders illustrate the cell type (IT:red; PT=blue) and layer analyzed. Experimental values derived from the control, MTh inactivation and NA-R block conditions indicated with small gray circle (remaining values were extrapolated) Model results include additional simulations covering the full parameter space explored. **B.** Same as in A but for different L5B cell types and subpopulations (IT, PT, PT5B_{upper} and PT5B_{lower}) each of which showed highly specific response patterns to MTh and NA.

332 Our model reproduced the pattern of M1 L5B in vivo responses observed experimentally for dif-
333 ferent levels of MTh and NA inputs, and provided insights and predictions of how the different L5B
334 subpopulations respond and interact (Fig. 6). The experimental and modeling results reported so
335 far suggest that M1 L5B response depends strongly on MTh and NA inputs. Fig. 6A shows the exper-
336 iment (top) and model (bottom) L5B mean firing rates as a function of these two inputs, illustrating
337 that MTh and NA inputs moderately increased the L5B response, but both are simultaneously re-
338 quired to trigger high L5B activity. Both experiment and model exhibit a similar response pattern,
339 progressively increasing with MTh and NA, and a similar range of L5B firing rates. We note that
340 these experimental results combine and extrapolate data from the control, MTh inactivation and
341 NA-R block conditions. The model results corresponds to the original version (without the modi-
342 fications proposed in the previous sections) but we included additional simulations covering the
343 full parameter space explored, i.e. all combinations of MTh input and NA modulation (PT I_h) values
344 (see Methods for details). To provide a better intuition of the full circuit model dynamics, we also
345 included the spiking raster plots for the 4 conditions with minimum and maximum MTh/NA values
346 (see arrows from the 4 corners of the model heatmap in Fig. 6A).

347 The model revealed highly specific and distinct activity patterns for the different L5B cell types
348 and sublayers (Fig. 6B). Somewhat surprisingly, L5B IT cells exhibited an inverse response pattern to
349 NA compared to L5B PT and to the overall L5B response (Fig. 6B), showing a decrease firing with
350 increases of MTh or NA inputs; and a largely constant response to MTh inputs. The NA response is
351 consistent with the low levels of I_h expression in L5B IT cells (*Sheets et al., 2011*). We hypothesize
352 the inverse response to NA between L5B IT and PT cells could be caused by mutual disinhibition
353 mediated via L5 interneurons. The lack of L5B IT response to MTh is consistent with the weak pro-
354 jections from MTh to deep IT neurons (*Yamawaki et al., 2015; Hooks et al., 2013*). L5B PT cells
355 showed higher peak firing rates than IT (12.8 Hz vs 7.4 Hz) thus dictating the overall L5B response
356 pattern and overshadowing L5 IT inverse pattern. Supragranular IT2/3 and IT5A populations exhib-
357 ited generally low activity (see Fig. 6A raster plots) when PT5B fired strongly (high MTh and NA), con-
358 sistent with their predominant role in motor preparation (*Li et al., 2015b*). The model also exposed
359 sublaminar differences in L5B PT response, with PT5B_{lower} exhibiting more extreme minimum and
360 maximum rates than PT5B_{upper} (0 – 15 Hz vs 3 – 10 Hz). The PT5B_{lower} activation threshold was also
361 higher than for PT5B_{upper}, i.e. it required higher MTh and NA values to start responding strongly.
362 This is consistent with the suggested role of PT5B_{upper} in movement preparation and PT5B_{lower} cells
363 in movement initiation (*Economo et al., 2018*).

364 Discussion

365 In this work we developed a computational model of the mouse M1 microcircuit and validated it
366 against in vivo data. Despite inherent limitations due to gaps in the data (see details in the section
367 below), we believe this constitutes the most biophysically detailed model of mouse M1 currently
368 available comprising the molecular, cellular and circuit scales. The model integrates quantitative ex-
369 perimental data on neuronal physiology, morphology, laminar density, cell type distribution, den-
370 dritic distribution of synapses, and local and long-range synaptic connectivity, obtained from 31
371 studies, with 12 of these coming from our experimental laboratory. Model development also ben-
372 efitied greatly from extended discussions between the computational and experimental authors.
373 Integrating data across scales and managing such a complex model motivated the development
374 of a novel software tool, NetPyNE, that provides a high-level interface to NEURON and facilitates
375 multiscale brain circuit modeling (*Dura-Bernal et al., 2019*).

376 To validate the model we focused on reproducing mouse M1 in vivo experimental results across
377 different behavioral states and experimental conditions from a single study (*Schiemann et al.,
378 2015*). Simulation results were largely consistent across multiple random wiring seeds and back-
379 ground input seeds demonstrating the robustness of the model. The model cell type-specific spon-
380 taneous firing rates, associated with the quiet behavior, were consistent with experimental data
381 from several in vivo studies (*Schiemann et al., 2015; Zagha et al., 2015; Li et al., 2016; Estebanez*

382 et al., 2018; Economo et al., 2018) (Fig. 2). We simulated activity corresponding to mouse self-
383 paced, voluntary locomotion through increased motor thalamus (MTh) and noradrenaline (NA) in-
384 puts. Movement-related changes in L2/3 and L5B population firing rates were consistent with those
385 reported in vivo, including bidirectional firing rate changes in distinct L5B pyramidal neurons popu-
386 lations (enhanced vs suppressed) (Fig. 3). Local field potentials (LFP) exhibited oscillations at phys-
387 iological frequencies, including delta, beta and gamma, which emerged spontaneously despite no
388 oscillatory inputs. LFP power in L5B shifted from lower (delta) to higher (gamma) frequency bands
389 during movement, consistent with in vivo LFP data (Fig. 4). We also simulated two experimental ma-
390 nipulations – inactivation of MTh and blocking of NA receptors – which resulted in cell type-specific
391 activity changes in L5B correspondent with those measured experimentally (Fig. 5). For each condi-
392 tion we evaluated two hypotheses of the cellular and circuit mechanisms involved, which suggested
393 MTh inactivation may affect other long-range inputs, and NA modulation affects not only I_h but
394 also K^+ conductances. We used the model to systematically explore the interaction between MTh
395 and NA inputs and predict M1 output at the level of individual cell types at sublaminar resolution.
396 Results captured the overall pattern and response amplitudes measured in vivo, supporting the
397 hypotheses both high MTh and NA inputs are required for self-paced voluntary movement-related
398 L5B activity (Fig. 6). The model predicted a predominant role of PT cells in dictating L5B responses
399 during movement, with $PT5B_{lower}$ providing the strongest response but only when both MTh and
400 NA inputs were high enough, i.e. $PT5B_{lower}$ exhibited the highest response threshold. L5B IT cells ex-
401 hibited an opposite but lower-amplitude pattern, potentially due to PT-mediated disinhibition, and
402 infragranular IT were less engaged during the movement state. These predictions are consistent
403 with findings associating IT and $PT5B_{upper}$ with motor planning and $PT5B_{lower}$ with motor execution
(Economo et al., 2018; Winnubst et al., 2019; Muñoz-Castañeda et al., 2021; Zhang et al., 2021).

404 This is, to the best of our knowledge, the first model of the mouse M1 microcircuit where fir-
405 ing rates and LFPs have been directly compared to cell type and layer-specific mouse M1 in vivo
406 data associated with different behaviors and experimental manipulations. The model provides a
407 quantitative theoretical framework to integrate and interpret M1 experimental data across scales,
408 evaluate hypotheses and generate experimentally testable predictions.

410 Challenges and limitations

411 Our ambition was to develop a detailed multiscale computational model of the mouse M1 micro-
412 circuit. We necessarily fell short due to lack of data on a number of key molecular, cellular, network
413 and long-range connectivity aspects. This model was constructed and evaluated over a period of
414 five years. During this period we updated the model multiple times to incorporate new data, but
415 of course any neurobiological model is always in need of additional updating and improvement as
416 new measurements become available.

417 Of some concern is the relative lack of data on dendritic ion channel density, which will affect the
418 influence of distal synaptic inputs on L5 neurons (**Labarrera et al., 2018**). Cell models are precisely
419 tuned to reproduce experimental somatic responses, but limited data is available to characterize
420 dendritic physiology. Although we adapted the morphology and physiology of IT cells based on
421 their layer, we omitted cellular diversity within each model population – all the model neurons of
422 the same cell type and layer have identical morphologies and identical channel parameters. This
423 contrasts with other models which vary both channel conductances and morphologies, the latter
424 by slightly jittering angles and lengths (**Markram et al., 2015a**).

425 Due to the nature of our circuit mapping methods (**Anderson et al., 2010; Hooks et al., 2013;**
426 Suter and Shepherd, 2015), our model used connection density based on postsynaptic cell type and
427 presynaptic locations. Our model's normalized cortical-depth-dependent connectivity provided
428 greater resolution than traditional layer-based wiring, but still contained boundaries where con-
429 nection density changed and did not provide cell level point-to-point resolution. This could be
430 further improved by fitting discretely binned experimental data to functions of cortical depth, re-
431 sulting in smoother connectivity profiles. Other recent models have used a sophisticated version

432 of Peters' principle (identifying overlap between axonal and dendritic trees) to provide cell-to-cell
433 resolution for selected cells, which must then still be replicated and generalized across multiple
434 instances to build a large network (*Rees et al., 2017; Markram et al., 2015a*).

435 We are limited not only by lack of precise data for parameter determination, but also by compu-
436 tational constraints. Often, network simulations use point neurons in order to avoid the computa-
437 tional load of multicompartment neurons, but at the expense of accuracy (*Potjans and Diesmann,*
438 *Izhikevich and Edelman, 2008; Schmidt et al., 2018*). Here, we compromised by using rela-
439 tively small multicompartment models for most populations, with the exception of the neurons
440 of L5. In terms of noradrenaline influence, we focused here on one effect on the PT cell type,
441 neglecting the wide-ranging effects of this and other neuromodulators (dopamine, acetylcholine)
442 (*O'Donnell et al., 2012; McCormick, 1992; Graybiel, 1990*) and their the influence of second mes-
443 senger cascades (*Neymotin et al., 2016a*). Implementing this functionality is now available via
444 NEURON's *rxd* module (*McDougal et al., 2013; Newton et al., 2018*). Even with these compromises,
445 optimizing and exploring our large network model required millions of HPC core-hours.

446 In summary, model firing rate distributions were generally consistent with experimental data
447 across populations and behavioral states. We note that the experimental dataset represents a
448 small sparse sample of neurons in the modeled cortical volume, resulting in the sample size of
449 model data was approximately 3 orders of magnitude larger than that of experiment (e.g. for L5B
450 $N_{model} = 35182$ vs $N_{experiment} = 47$). Therefore, validation of our model results can be understood
451 as showing that the small dataset of experiment cell rates could have been subsampled from the
452 larger dataset of model rates. Novel methods that record from an increasingly larger number
453 of simultaneous neurons (*Hong and Lieber, 2019*) will enable additional validation of the model
454 results.

455 **M1 cellular and circuit mechanisms associated with quiet and movement behav- 456 iors**

457 A key question in motor system research is how motor cortex activity gets dissociated from muscle
458 movement during motor planning or mental imagery, and is then shifted to produce commands for
459 action (*Ebbesen and Brecht, 2017; Schieber, 2011*). One hypothesis has been that this planning-to-
460 execution switch might be triggered by NA neuromodulation (*Sheets et al., 2011*). Downregulation
461 of I_h , effected via NA and other neuromodulatory factors, has been shown to increase PT activity
462 as a consequence of enhanced temporal and spatial synaptic integration of EPSPs (*Sheets et al.,*
463 *2011; Labarrera et al., 2018*). This effect is primarily observed in PT cells, since the concentration of
464 HCN channels in these cells has been shown to be significantly higher than in IT cells (*Sheets et al.,*
465 *2011; Hay et al., 2011*). In the model we assumed the baseline I_h to correspond to that of the cell
466 tuned to reproduce in vitro data (no NA modulation). For the in vivo quiet condition (low NA mod-
467 ulation) we used 75% of that baseline level, and for movement (high NA) we used 25%, consistent
468 with values reported experimentally (*Labarrera et al., 2018*). Paradoxically, I_h downregulation has
469 also been reported to reduce pyramidal cell activity in some settings (*George et al., 2009; Migliore*
470 *and Migliore, 2012*). Here we improved our previous PT cell model (*Neymotin et al., 2017*) to in-
471 clude an I_h model (*Migliore and Migliore, 2012*) that was able to reconcile these observations: I_h
472 downregulation reduced PT response to weak inputs, while increasing the cell response to strong
473 inputs (*Migliore and Migliore, 2012; George et al., 2009; Sheets et al., 2011; Labarrera et al., 2018*).

474 An additional hypothesis is that differential planning and movement outputs would result from
475 activation of different cells in L5 (*Yu et al., 2008; Anderson et al., 2010; Hooks et al., 2013*) mediated
476 by distinct local and long-range inputs. Accumulated evidence suggests inputs arising from MTh (i.e.
477 ventrolateral (VL) thalamus) carrying cerebellar signals differentially target M1 populations (*Hooks*
478 *et al., 2013*) and are involved in triggering movement (*Dacre et al., 2021*) and in dexterous tasks
479 (*Guo et al., 2021*). Further support for this hypothesis comes from a study that transcriptomically
480 identified different PT subtypes in upper vs lower L5B (*Economo et al., 2018*), and showed that
481 PT5B_{upper} projected to thalamus and generated early preparatory activity, while PT5B_{lower} projected

482 to medulla and generated motor commands.

483 These two hypotheses are not incompatible, and indeed our simulations suggest both of these
484 mechanisms may coexist and be required for movement-related activity (Fig. 6). NA modulation
485 and MTh input by themselves produced an increase in PT5B overall activity, but primarily in the
486 preparatory activity-related PT5B_{upper} population; both mechanisms were required to activate the
487 PT5B_{lower} population associated with motor commands (*Economou et al., 2018*). The model there-
488 fore predicts that the transition to motor execution (self-paced, voluntary movement) might re-
489 quire both the neuromodulatory prepared state and circuit-level routing of inputs. Different types
490 of behaviors and contexts (e.g. goal-directed behaviors with sensory feedback) may involve driving
491 inputs from other populations or regions, such as supragranular layers or somatosensory cortex
492 (*Hooks et al., 2013; Dacre et al., 2021; Zareian et al., 2021; Muñoz-Castañeda et al., 2021*). We ac-
493 knowledge that the quiet state in the model (and experimental data (*Schiemann et al., 2015*) does
494 not correspond to a preparatory state, as it lacks short-term memory, delays and other prepara-
495 tory components; and hence generalizing previous task-related findings (*Economou et al., 2018*) on
496 the role of PT5B_{lower} and PT5B_{upper} to interpret our voluntary movement-specific results may be
497 inadequate.

498 **Simulating experimental manipulations: motor thalamus inactivation and nora- 499 drenaline blocking**

500 Attempting to reproduce the extreme conditions posed by experimental manipulations provided
501 further insights into the circuitry and mechanisms governing M1 dynamics. During MTh inactiva-
502 tion, our baseline model exhibited higher firing rates than *in vivo*, particularly for the quiet state.
503 We hypothesized this may be due to inactivation of MTh (VL) also affecting other afferent regions
504 of M1, such as contralateral M1 and S2; either directly (e.g. VL→S2) and/or indirectly via recurrent
505 interareal projections (e.g. M1→S2→M1). We evaluated this by reducing activity in these model
506 regions, which indeed resulted in a closer match to *in vivo* rates (Fig. 5). Several other hypoth-
507 eses may also explain the observed discrepancies, for example, that movement-related activity 1)
508 depends on changes in spiking patterns and not just amplitude (e.g. bursts or oscillatory activ-
509 ity); or 2) that it is driven not only by VL but by other long-range inputs (consistent with recent
510 findings (*Dacre et al., 2021*)), and/or by local lateral inputs from non-modeled regions of M1. The
511 inclusion of detailed interactions among afferent cortical and thalamic regions is out of the scope
512 of this paper. However, our results already suggested possible improvements to the model and
513 circuit pathways to explore experimentally, demonstrating that the model can be used to evaluate
514 different candidate circuitries and activity patterns.

515 Similarly, for the NA receptor block condition, we modified the model to evaluate the hypothesis
516 that it not only increases PT I_h but also K⁺ conductance in all pyramidal neurons, as suggested
517 by multiple studies (*Wang and McCormick, 1993; Favero et al., 2012*). This resulted in a closer
518 match between model and experiment. Alternative hypotheses that may also account for the initial
519 differences observed include NA selective modulation of inhibitory synapses, and interactions with
520 other neuromodulators such as acetylcholine (*Conner et al., 2010*). These molecular and cellular
521 level mechanisms can be explored in our model to gain insights into their circuit-level effects.

522 **Emergence of behavior-dependent physiological oscillations**

523 Our model of M1 neocortex exhibits spontaneous physiological oscillations without rhythmogenic
524 synaptic input. Strong oscillations were observed in the delta and beta/gamma ranges with specific
525 frequency-dependence on cell class and cortical depth. Strong LFP beta and gamma oscillations
526 are characteristic of motor cortex activity in both rodents (*Castro-Alamancos, 2013; Tsubo et al.,
527 2013*) and primates (*Rubino et al., 2006; Nishimura et al., 2013*), and have been found to enhance
528 signal transmission in mouse neocortex (*Sohal et al., 2009*). Both beta and gamma oscillations
529 may play a role in information coding during preparation and execution of movements (*Ainsworth
530 et al., 2012; Tsubo et al., 2013*). More generally, these physiological oscillations are considered to

531 be fundamental to the relation of brain structure and function (*Buzsáki and Mizuseki, 2014*). As
532 the primary output, PT cells receive and integrate many local and long-range inputs. Their only
533 local connections to other L5 excitatory neurons are to other PT cells (*Kiritani et al., 2012*). How-
534 ever, by targeting inhibitory cells in L5, (*Apicella et al., 2012*) they are able to reach across layers
535 to influence other excitatory populations, either reducing activity or entraining activity (*Naka and*
536 *Adesnik, 2016*). These disynaptic E→I→E pathways likely play a role in coupling oscillations within
537 and across layers, and in setting frequency bands.

538 **Implications for experimental research and therapeutics**

539 Our model integrates previously isolated experimental data at multiple scales into a unified simu-
540 lation that can be progressively extended as new data becomes available. This provides a useful
541 tool for researchers in the field, who can use this quantitative theoretical framework to evaluate
542 hypotheses, make predictions and guide the design of new experiments using our freely-available
543 model (see Methods). This *in silico* testbed can be systematically probed to study microcircuit
544 dynamics and biophysical mechanisms with a level of resolution and precision not available ex-
545 perimentally. Unraveling the non-intuitive multiscale interactions occurring in M1 circuits can help
546 us understand disease and develop new pharmacological and neurostimulation treatments for
547 brain disorders (*Neymotin et al., 2016c,b; Dura-Bernal et al., 2016; Arle and Shils, 2008; Wang*
548 *et al., 2015; Bensmaia and Miller, 2014; Sanchez et al., 2012*), and improve decoding methods for
549 brain-machine interfaces (*Carmena, 2013; Shenoy and Carmena, 2014; Dura-Bernal et al., 2017;*
550 *Kocaturk et al., 2015*).

551 **Methods**

552 The methods below describe model development with data provenance, and major aspects of
553 the final model. The full documentation of the final model is the source code itself, available for
554 download at <http://modeldb.yale.edu/260015>.

555 **Morphology and physiology of neuron classes**

556 Seven excitatory pyramidal cell and two interneuron cell models were employed in the network.
557 Their morphology and physiological responses are summarized in Figs. 1A,B,C and 7. In previ-
558 ous work we developed layer 5B PT corticospinal cell and L5 IT corticostratal cell models that re-
559 produced *in vitro* electrophysiological responses to somatic current injections, including sub- and
560 super-threshold voltage trajectories and f-I curves (*Neymotin et al., 2017; Suter et al., 2013*). To
561 achieve this, we optimized the parameters of the Hodgkin-Huxley neuron model ionic channels –
562 Na, Kdr, Ka, Kd, HCN, CaL, CaN, KCa – within a range of values constrained by the literature. The
563 corticospinal and corticostratal cell model morphologies had 706 and 325 compartments, respec-
564 tively, digitally reconstructed from 3D microscopy images. Morphologies are available via Neuro-
565 Morpho.org (*Ascoli et al., 2007*) (archive name “Suter_Shepherd”). For the current simulations, we
566 further improved the PT model by 1) increasing the concentration of Ca²⁺ channels (“hot zones”)
567 between the nexus and apical tuft, following parameters published in (*Hay et al., 2011*); 2) low-
568 ering dendritic Na⁺ channel density in order to increase the threshold required to elicit dendritic
569 spikes, which then required adapting the axon sodium conductance and axial resistance to main-
570 tain a similar f-I curve; 3) replacing the HCN channel model and distribution with a more recent
571 implementation (*Migliore and Migliore, 2012*). The new HCN channel reproduced a wider range
572 of experimental observations than our previous implementation (*Kole et al., 2006*), including the
573 change from excitatory to inhibitory effect in response to synaptic inputs of increasing strength
574 (*George et al., 2009*). This was achieved by including a shunting current proportional to I_h . We
575 tuned the HCN parameters (I_h and v_{rev,I_h}) and passive parameters to reproduce the findings noted
576 above, while keeping a consistent f-I curve consistent (*Suter et al., 2013*).

577 The network model includes five other excitatory cell classes: layer 2/3, layer 4, layer 5B and
578 layer 6 IT neurons and layer 6 CT neurons. Since our focus was on the role of L5 neurons, other cell

579 classes were implemented using simpler models as a trade-off to enable running a larger number
580 of exploratory network simulations. Previously we had optimized 6-compartment neuron models
581 to reproduce somatic current clamp recordings from two IT cells in layers 5A and 5B. The layer 5A
582 cell had a lower f-I slope (77 Hz/nA) and higher rheobase (250 nA) than that in layer 5B (98 Hz/nA
583 and 100 nA). Based on our own and published data, we found two broad IT categories based on
584 projection and intrinsic properties: corticocortical IT cells found in upper layers 2/3 and 4 which
585 exhibited a lower f-I slope (~72 Hz/nA) and higher rheobase (~281 pA) than IT corticostriatal cells
586 in deeper layers 5A, 5B and 6 (~96 Hz/nA and ~106 pA) (*Yamawaki et al., 2015; Suter et al., 2013;*
587 *Oswald et al., 2013*). CT neurons' f-I rheobase and slope (69 Hz/nA and 298 pA) was closer to that
588 of corticocortical neurons (*Oswald et al., 2013*). We therefore employed the layer 5A IT model for
589 layers 2/3 and 4 IT neurons and layer 6 CT neurons, and the layer 5B IT model for layers 5A, 5B and
590 6 IT neurons. We further adapted cell models by modifying their apical dendrite length to match
591 the average cortical depth of the layer, thus introducing small variations in the firing responses of
592 neurons across layers.

593 We implemented models for two major classes of GABAergic interneurons (*Harris and Shep-
594 herd, 2015*): parvalbumin-expressing fast-spiking (PV) and somatostatin-expressing low-threshold
595 spiking neurons (SOM). We employed existing simplified 3-compartment (soma, axon, dendrite)
596 models (*Konstantoudaki et al., 2014*) and increased their dendritic length to better match the av-
597 erage f-I slope and rheobase experimental values of cortical basket (PV) and Martinotti (SOM) cells
598 (Neuroelectro online database (*Tripathy et al., 2015*)).

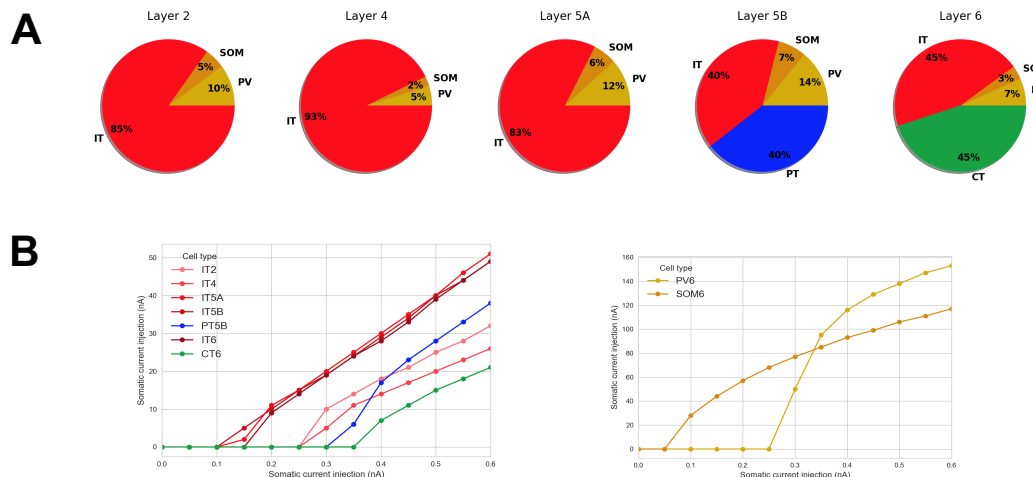


Figure 7. Microcircuit layer composition and cell type f-I response. **A.** Proportion of cell classes per layer;
B. f-I curve for each excitatory and inhibitory cell types. All properties were derived from published
experimental data. Populations labels include the cell class and layer, e.g. 'IT2' represents the IT class neurons
in layer 2/3.

599 Microcircuit composition: neuron locations, densities and ratios

600 We modeled a cylindric volume of the mouse M1 cortical microcircuit with a 300 μm diameter and
601 1350 μm height (cortical depth) at full neuronal density for a total of 10,073 neurons (Fig. 1). Cylin-
602 der diameter was chosen to approximately match the horizontal dendritic span of a corticospinal
603 neuron located at the center, consistent with the approach used in the Human Brain Project model
604 of the rat S1 microcircuit (*Markram et al., 2015b*). Mouse cortical depth and boundaries for layers
605 2/3, 4, 5A, 5B and 6 were based on our published experimental data (*Weiler et al., 2008; Anderson
606 et al., 2010; Yamawaki et al., 2015*). Although traditionally M1 has been considered an agranular
607 area lacking layer 4, we recently identified M1 pyramidal neurons with the expected prototypical
608 physiological, morphological and wiring properties of layer 4 neurons (*Yamawaki et al., 2015*) (see

609 also (*Bopp et al., 2017; Barbas and García-Cabezas, 2015*)), and therefore incorporated this layer
610 in the model.

611 Cell classes present in each layer were determined based on mouse M1 studies (*Harris and*
612 *Shepherd, 2015; Suter et al., 2013; Anderson et al., 2010; Yamawaki et al., 2015; Oswald et al.,*
613 *2013; Konstantoudaki et al., 2014; Naka and Adesnik, 2016*). IT cell populations were present in
614 all layers, whereas the PT cell population was confined to layer 5B, and the CT cell population only
615 occupied layer 6. SOM and PV interneuron populations were distributed in each layer. Neuronal
616 densities (neurons per mm³) for each layer (Fig. 1C) were taken from a histological and imaging study
617 of mouse agranular cortex (*Tsai et al., 2009*). The proportion of excitatory to inhibitory neurons
618 per layer was obtained from mouse S1 data (*Lefort et al., 2009*). The proportion of IT to PT and IT
619 to CT cells in layers 5B and 6, respectively, were both estimated as 1:1 (*Harris and Shepherd, 2015;*
620 *Suter et al., 2013; Yamawaki and Shepherd, 2015*). The ratio of PV to SOM neurons per layer was
621 estimated as 2:1 based on mouse M1 and S1 studies (*Katzel et al., 2011; Wall et al., 2016*) (Fig. 7B).
622 Since data for M1 layer 4 was not available, interneuron populations labeled PV5A and SOM5A
623 occupy both layers 4 and 5A. The number of cells for each population was calculated based on the
624 modeled cylinder dimensions, layer boundaries and neuronal proportions and densities per layer.

625 Local connectivity

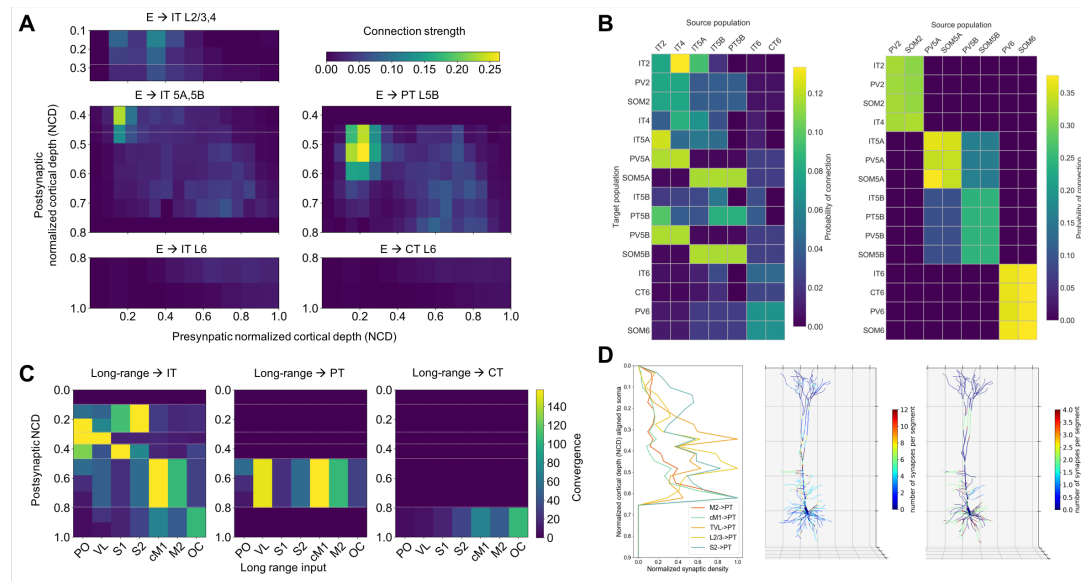


Figure 8. M1 excitatory connectivity: local microcircuitry and long-range inputs. **A.** Strength of local excitatory connections as a function of pre- and post-synaptic normalized cortical depth (NCD) and post-synaptic cell class; values used to construct the network. **B.** Convergence of long-range excitatory inputs from seven thalamic and cortical regions as a function post-synaptic NCD and cell class; values used to construct the network. **C.** Probability of connection matrix for excitatory (left) and inhibitory (right) populations calculated from an instantiation of the base model network. **D.** Left. Synaptic density profile (1D) along the dendritic arbor for inputs from layer 2/3 IT, VL, S1, S2, cM1 and M2 to PT neurons. Calculated by normalizing sCRACM maps (*Suter and Shepherd, 2015*) Figs. 5 and 6 by dendritic length at each grid location and averaging across rows. Middle and Right. Synaptic density per neuron segment automatically calculated for each neuron based on its morphology and the pre- and postsynaptic cell type-specific radial synaptic density function. Here, VL → PT and S2 → PT are compared and exhibit partially complementary distributions.

626 We calculated local connectivity between M1 neurons (Figures 1C and 8A) by combining data
627 from multiple studies. Data on excitatory inputs to excitatory neurons (IT, PT and CT) was pri-
628 marily derived from mapping studies using whole-cell recording, glutamate uncaging-based laser-
629 scanning photostimulation (LSPS) and subcellular channelrhodopsin-2-assisted circuit mapping
630 (sCRACM) analysis (*Weiler et al., 2008; Anderson et al., 2010; Yamawaki et al., 2015; Yamawaki*

631 *and Shepherd, 2015*). Connectivity data was postsynaptic cell class-specific and employed normalized
632 cortical depth (NCD) instead of layers as the primary reference system. Unlike layer definitions
633 which can be interpreted differently between studies, NCD provides a well-defined, consistent and
634 continuous reference system, depending only on two readily-identifiable landmarks: pia (NCD=0)
635 and white matter (NCD=1). Incorporating NCD-based connectivity into our model allowed us to
636 capture wiring patterns down to a 100 μm spatial resolution, well beyond traditional layer-based
637 cortical models. M1 connectivity varied systematically within layers. For example, the strength of
638 inputs from layer 2/3 to L5B corticospinal cells depends significantly on cell soma depth, with upper
639 neurons receiving much stronger input (*Anderson et al., 2010*).

640 Connection strength thus depended on presynaptic NCD and postsynaptic NCD and cell class.
641 For postsynaptic IT neurons with NCD ranging from 0.1 to 0.37 (layers 2/3 and 4) and 0.8 to 1.0
642 (layer 6) we determined connection strengths based on data from (*Weiler et al., 2008*) with cortical
643 depth resolution of 140 μm -resolution. For postsynaptic IT and PT neurons with NCD between 0.37
644 and 0.8 (layers 5A and 5B) we employed connectivity strength data from (*Anderson et al., 2010*)
645 with cortical depth resolution of 100 μm . For postsynaptic CT neurons in layer 6 we used the same
646 connection strengths as for layer 6 IT cells (*Weiler et al., 2008*), but reduced to 62% of original values,
647 following published data on the circuitry of M1 CT neurons (*Yamawaki and Shepherd, 2015*). Our
648 data (*Yamawaki and Shepherd, 2015*) also suggested that connection strength from layer 4 to layer
649 2/3 IT cells was similar to that measured in S1, so for these projections we employed values from
650 Lefort's S1 connectivity strength matrix (*Lefort et al., 2009*). Experimentally, these connections
651 were found to be four times stronger than in the opposite direction – from layer 2/3 to layer 4 – so
652 we decreased the latter in the model to match this ratio.

653 Following previous publications (*Kiritani et al., 2012; Lefort et al., 2009*), we defined connection
654 strength (s_{con} , in mV) between two populations, as the product of their probability of connection
655 (p_{con}) and the unitary connection somatic EPSP amplitude in mV (v_{con}), i.e. $s_{con} = p_{con} \times v_{con}$. We
656 employed this equivalence to disentangle the connection s_{con} values provided by the above LSFS
657 studies into p_{con} and v_{con} values that we could use to implement the model. First, we rescaled the
658 LSFS raw current values in pA (*Anderson et al., 2010; Weiler et al., 2008; Yamawaki et al., 2015;*
659 *Yamawaki and Shepherd, 2015*) to match s_{con} data from a paired recording study of mouse M1
660 L5 excitatory circuits (*Kiritani et al., 2012*). Next, we calculated the M1 NCD-based v_{con} matrix by
661 interpolating a layerwise unitary connection EPSP amplitude matrix of mouse S1 (*Lefort et al.,
662 2009*), and thresholding values between 0.3 and 1.0 mV. Finally, we calculated the probability of
663 connection matrix as $p_{con} = s_{con}/v_{con}$.

664 To implement v_{con} values in the model we calculated the required NEURON connection weight
665 of an excitatory synaptic input to generate a somatic EPSP of 0.5 mV at each neuron segment.
666 This allowed us to calculate a scaling factor for each segment that converted v_{con} values into NEU-
667 RON weights, such that the somatic EPSP response to a unitary connection input was independent
668 of synaptic location – also known as synaptic democracy (*Rumsey and Abbott, 2006; Poirazi and
669 Papoutsi, 2020*). This is consistent with experimental evidence showing synaptic conductances in-
670 creased with distance from soma, to normalize somatic EPSP amplitude of inputs within 300 μm
671 of soma (*Magee and Cook, 2000*). Following this study, scaling factor values above 4.0 – such as
672 those calculated for PT cell apical tufts – were thresholded to avoid overexcitability in the network
673 context where each cell receives hundreds of inputs that interact nonlinearly (*Spruston, 2008; Be-
674 habadi et al., 2012*). For morphologically detailed cells (layer 5A IT and layer 5B PT), the number
675 of synaptic contacts per unitary connection (or simply, synapses per connection) was set to five,
676 an estimated average consistent with the limited mouse M1 data (*Hu and Agmon, 2016*) and rat
677 S1 studies (*Bruno and Sakmann, 2006; Markram et al., 2015b*). Individual synaptic weights were
678 calculated by dividing the unitary connection weight (v_{con}) by the number of synapses per connec-
679 tion. Although the method does not account for nonlinear summation effects (*Spruston, 2008*), it
680 provides a reasonable approximation and enables employing a more realistic number and spatial
681 distribution of synapses, which may be key for dendritic computations (*London and Häusser, 2005*).

682 For the remaining cell models, all with six compartments or less, a single synapse per connection
683 was used.

684 For excitatory inputs to inhibitory cell types (PV and SOM) we started with the same values as
685 for IT cell types but adapted these based on the specific connectivity patterns reported for mouse
686 M1 interneurons (*Apicella et al., 2012; Yamawaki and Shepherd, 2015*) (Fig. 8A). Following the
687 layer-based description in these studies, we employed three major subdivisions: layer 2/3 (NCD
688 0.12 to 0.31), layers 4, 5A and 5B (NCD 0.31 to 0.77) and layer 6 (NCD 0.77 to 1.0). We increased
689 the probability of layer 2/3 excitatory connections to layers 4, 5A and 5B SOM cells by 50% and
690 decreased that to PV cells by 50% (*Apicella et al., 2012*). We implemented the opposite pattern
691 for excitatory connections arising from layer 4,5A,5B IT cells such that PV interneurons received
692 stronger intralaminar inputs than SOM cells (*Apicella et al., 2012*). The model also accounts for
693 layer 6 CT neurons generating relatively more inhibition than IT neurons (*Yamawaki and Shepherd,*
694 *2015*). Inhibitory connections from interneurons (PV and SOM) to other cell types were limited to
695 neurons in the same layer (*Katzel et al., 2011*), with layers 4, 5A and 5B combined into a single
696 layer (*Naka and Adesnik, 2016*). Probability of connection decayed exponentially with the distance
697 between the pre- and post-synaptic cell bodies with length constant of 100 μm (*Gal et al., 2017;*
698 *Fino and Yuste, 2011*). We introduced a correction factor to the distance-dependent connectivity
699 measures to avoid the *border effect*, i.e. cells near the modeled volume edges receiving less or
700 weaker connections than those in the center.

701 For comparison with other models and experiments, we calculated the probability of connec-
702 tion matrices arranged by population (instead of NCD) for the base model network instantiation
703 used throughout the results. (Fig. 8B).

704 Excitatory synapses consisted of colocalized AMPA (rise, decay τ : 0.05, 5.3 ms) and NMDA (rise,
705 decay τ : 15, 150 ms) receptors, both with reversal potential of 0 mV. The ratio of NMDA to AMPA re-
706 ceptors was 1.0 (*Myne et al., 2003*), meaning their weights were each set to 50% of the connection
707 weight. NMDA conductance was scaled by $1/(1 + 0.28 \cdot Mg \cdot \exp(-0.062 \cdot V))$; Mg = 1 mM (*Jahr and*
708 *Stevens, 1990b*). Inhibitory synapses from SOM to excitatory neurons consisted of a slow *GABA_A*
709 receptor (rise, decay τ : 2, 100 ms) and *GABA_B* receptor, in a 90% to 10% proportion; synapses from
710 SOM to inhibitory neurons only included the slow *GABA_A* receptor; and synapses from PV to other
711 neurons consisted of a fast *GABA_A* receptor (rise, decay τ : 0.07, 18.2). The reversal potential was
712 -80 mV for *GABA_A* and -95 mV for *GABA_B*. The *GABA_B* synapse was modeled using second mes-
713 senger connectivity to a G protein-coupled inwardly-rectifying potassium channel (GIRK) (*Destexhe*
714 *et al., 1996*). The remaining synapses were modeled with a double-exponential mechanism.

715 Connection delays were estimated as 2 ms plus a variable delay depending on the distance
716 between the pre- and postsynaptic cell bodies assuming a propagation speed of 0.5 m/s.

717 Long-range input connectivity

718 We added long-range input connections from seven regions that are known to project to M1: tha-
719 lamic posterior nucleus (PO), ventro-lateral thalamus (VL), primary somatosensory cortex (S1), sec-
720 ondary somatosensory cortex (S2), contralateral primary motor cortex (cM1), secondary motor
721 cortex (M2) and orbital cortex (OC). Each region consisted of a population of 1000 (*Constantinople*
722 *and Bruno, 2013; Bruno and Sakmann, 2006*) spike-generators (NEURON VecStims) that generated
723 independent random Poisson spike trains with uniform distributed rates between 0 and 2.5 Hz or
724 0 and 5 Hz (*Yamashita et al., 2013; Hirata and Castro-Alamancos, 2006*) for spontaneous firing;
725 or 0 and 10 Hz (*Isomura et al., 2009; Jacob et al., 2012*) when simulating increased input from
726 a region. Previous studies provided a measure of normalized input strength from these regions
727 as a function of postsynaptic cell type and layer or NCD. Broadly, PO (*Yamawaki et al., 2015; Ya-*
728 *mawaki and Shepherd, 2015; Hooks et al., 2013*), S1 (*Mao et al., 2011; Yamawaki et al., 2021*) and
729 S2 (*Suter and Shepherd, 2015*) projected strongly to IT cells in layers 2/3 and 5A (PO also to layer
730 4); VL projected strongly to PT cells and to layer 4 IT cells (*Yamawaki et al., 2015; Yamawaki and*
731 *Shepherd, 2015; Hooks et al., 2013*); cM1 and M2 projected strongly to IT and PT cells in layers 5B

732 and 6 (**Hooks et al., 2013**); and OC projected strongly to layer 6 CT and IT cells (**Hooks et al., 2013**).
733 We implemented these relations by estimating the maximum number of synaptic inputs from each
734 region and multiplying that value by the normalized input strength for each postsynaptic cell type
735 and NCD range. This resulted in a convergence value – average number of synaptic inputs to each
736 postsynaptic cell – for each projection Fig. 8C. We fixed all connection weights (unitary connection
737 somatic EPSP amplitude) to 0.5 mV, consistent with rat and mouse S1 data (**Hu and Agmon, 2016**;
738 **Constantinople and Bruno, 2013**).

739 To estimate the maximum number of synaptic inputs per region, we made a number of as-
740 sumptions based on the limited data available (Figs. 8C and 1C). First, we estimated the average
741 number of synaptic contacts per cell as 8234 by rescaling rat S1 data (**Meyer et al., 2010b**) based
742 on our own observations for PT cells (**Suter et al., 2013**) and contrasting with related studies (**Schüz**
743 and **Palm, 1989**; **DeFelipe et al., 2002**); we assumed the same value for all cell types so we could use
744 convergence to approximate long-range input strength. We assumed 80 % of synaptic inputs were
745 excitatory vs. 20 % inhibitory (**DeFelipe et al., 2002**; **Markram et al., 2015b**); out of the excitatory
746 inputs, 80 % were long-range vs. 20 % local (**Markram et al., 2015b**; **Stepanyants et al., 2009**); and
747 out of the inhibitory inputs, 30 % were long-range vs. 70 % local (**Stepanyants et al., 2009**). Finally,
748 we estimated the percentage of long-range synaptic inputs arriving from each region based on
749 mouse brain mesoscale connectivity data (**Oh et al., 2014**) and other studies (**Meyer et al., 2010a**;
750 **Bruno and Sakmann, 2006**; **Meyer et al., 2010b**; **Zhang et al., 2016**; **Bopp et al., 2017**).

751 Experimental evidence demonstrates the location of synapses along dendritic trees follows very
752 specific patterns of organization that depend on the brain region, cell type and cortical depth (**Pe-**
753 **treanu et al., 2009**; **Suter and Shepherd, 2015**); these are likely to result in important functional
754 effects (**Kubota et al., 2015**; **Laudanski et al., 2014**; **Spruston, 2008**). We employed sCRACM data to
755 estimate the synaptic density along the dendritic arbor – 1D radial axis – for inputs from PO, VL, M2
756 and OC to layers 2/3, 5A, 5B and 6 IT and CT cell (**Hooks et al., 2013**), and from layer 2/3 IT, VL, S1,
757 S2, cM1 and M2 to PT neurons (**Suter and Shepherd, 2015**) (Fig. 8D). To approximate radial synap-
758 tic density we divided the sCRACM map amplitudes by the dendritic length at each grid location,
759 and averaged across rows. Once all network connections had been generated, synaptic locations
760 were automatically calculated for each cell based on its morphology and the pre- and postsynaptic
761 cell type-specific radial synaptic density function (Fig. 8D). Synaptic inputs from PV to excitatory
762 cells were located perisomatically (50 μm around soma); SOM inputs targeted apical dendrites of
763 excitatory neurons (**Naka and Adesnik, 2016**; **Katzel et al., 2011**); and all inputs to PV and SOM cells
764 targeted apical dendrites. For projections where no data synaptic distribution data was available –
765 IT/CT, S1, S2 and cM1 to IT/CT cells – we assumed a uniform dendritic length distribution.

766 Model implementation, simulation and analysis

767 Modeling and simulation tools

768 The model was developed using parallel NEURON (neuron.yale.edu) (**Lytton et al., 2016**) and Net-
769 PyNE (www.netpyne.org) (**Dura-Bernal et al., 2019**), a Python package to facilitate the development
770 of biological neuronal networks in the NEURON simulator. NetPyNE emphasizes the incorpo-
771 ration of multiscale anatomical and physiological data at varying levels of detail. It converts a set of
772 simple, standardized high-level specifications in a declarative format into a NEURON model. This
773 high-level language enables, for example, defining connectivity as function of NCD, and distributing
774 synapses across neurons based on normalized synaptic density maps. NetPyNE facilitates running
775 parallel simulations by taking care of distributing the workload and gathering data across comput-
776 ing nodes, and automates the submission of batches of simulations for parameter optimization
777 and exploration. It also provides a powerful set of analysis methods so the user can plot spike
778 raster plots, LFP power spectra, information transfer measures, connectivity matrices, or intrinsic
779 time-varying variables (eg. voltage) of any subset of cells. To facilitate data sharing, the package
780 saves and loads the specifications, network, and simulation results using common file formats
781 (Pickle, Matlab, JSON or HDF5), and can convert to and from NeuroML (**Gleeson et al., 2010, 2019**)

782 and SONATA (*Dai et al., 2019*), standard data formats for exchanging models in computational
783 neuroscience. Simulations were run on XSEDE supercomputers Comet and Stampede, using the
784 Neuroscience Gateway (NSG) and our own resource allocation, and on Google Cloud supercom-
785 puters.

786 Parameter exploration/optimization

787 NetPyNE facilitates optimization and exploration of network parameters through automated batch
788 simulations. The user specifies the range of parameters and parameter values to explore and the
789 tool automatically submits the jobs in multicore machines (using NEURON's Bulletin board) or HPCs
790 (using SLURM/Torque). Multiple pre-defined batch simulation setups can be fully customized for
791 different environments. We ran batch simulations using NetPyNE's automated SLURM job submis-
792 sion on San Diego Supercomputer Center's (SDSC) Comet supercomputer and on Google Cloud
793 Platform.

794 Local Field Potentials

795 The NetPyNE tool also includes the ability to simulate local field potentials (LFPs) obtained from
796 extracellular electrodes located at arbitrary 3D locations within the network. The LFP signal at each
797 electrode is obtained using the "line source approximation" (*Parasuram et al., 2016; Buzsáki et al.,*
798 *2012; Lindén et al., 2013*), which is based on the sum of the membrane current source generated at
799 each cell segment divided by the distance between the segment and the electrode. The calculation
800 assumes that the electric conductivity and permittivity of the extracellular medium are constant
801 everywhere and do not depend on frequency.

802 Firing rates statistics

803 Firing rate statistics were always calculated starting at least 1 second after the simulation start time
804 to allow the network to reach a steady state. To enable the statistical comparison of the results in
805 Fig. 2 we only included neurons with firing rates above 0 Hz, given that most experimental datasets
806 (*Estebanez et al., 2018; Zagha et al., 2015; Li et al., 2015a*) already included this constraint. For the
807 statistical comparison in the remaining sections we included neurons with firing rates of 0 Hz, as
808 these were available both in the experimental dataset (*Schiemann et al., 2015*) and the model.
809 Therefore, the quiet state mean firing rates reported in Fig. 2 (which only included rates > 0 Hz)
810 were higher than those in the remaining sections.

811 Experimental procedures

812 Details of the experimental procedures used to obtain the data in this study were previously de-
813 scribed in (*Schiemann et al., 2015*), including animals and surgery, motion index and motion pat-
814 tern discrimination, and in vivo electrophysiology and pharmacology. The dataset on cell type-
815 specific in vivo firing rates across states and conditions was collected and previously reported in
816 the same publication. The LFP experimental data reported here was collected during that same
817 study but only a small subset was reported in the experimental paper ((*Schiemann et al., 2015*) Fig.
818 1)

819 The experimental LFP data used in Fig. 4 was preprocessed to remove outliers and potential
820 artifacts. The raw LFP data consisted of 30 recordings of varying duration during head-restrained
821 mice locomotion (at different speeds) on a cylindrical runged treadmill. In order to compare it
822 to the simulated data, the quiet in vivo raw LFP were classified into quiet and movement peri-
823 ods (using the same criteria as in (*Schiemann et al., 2015*)) and then segmented into 4-second
824 samples. We then calculated the LFP power spectral density (PSD) using the Morlet wavelet trans-
825 form method, normalized within each sample and computed the mean power for five standard
826 frequency bands (delta, theta, alpha, beta and gamma). The resulting dataset of 5-element vec-
827 tors (normalized power in each frequency band) exhibited high variability: the mean coefficient
828 of variation (CV) across quiet samples was 0.60 and 0.44 for move samples. Therefore we used k-
829 means to cluster the dataset. The quiet condition resulted in one predominant cluster with similar

power for all bands (73% of samples), and one with higher gamma power (27% of samples). Conversely, the move condition predominant cluster exhibited significantly higher gamma power (77% of samples), whereas the smaller cluster showed similar power across bands (23%). As expected, the variability within each cluster was significantly reduced compared to the full dataset (large clusters: quiet CV=0.33, move CV=0.32; small clusters: quiet CV=0.31, move CV=0.28). For comparison with the model results we employed the large quiet and move clusters (with over 70% of samples) (Fig. 4). The smaller clusters may correspond to different internal states during behavior, recording from regions/layers with different levels of involvement in the behavior, transition periods, and/or experimental artifacts (e.g. inaccurate segmenting of behavior).

839 Acknowledgements

840 This work was funded by the following grants: NIH U01EB017695 (WWL), NYS SCIRB DOH01-C32250GG-
841 3450000 (SDB,WWL), NIH U24EB028998 (SDB), NSF 1904444-1042C (SDB,WWL), NIH R01EB022903
842 (WWL), NIH R01DC012947 (SAN), ARO W911NF-19-1-0402 (SAN). The views and conclusions con-
843 tained in this document are those of the authors and should not be interpreted as representing
844 the official policies, either expressed or implied, of the U.S. Government or any of its agencies.
845 The U.S. Government is authorized to reproduce and distribute reprints for Government purposes
846 notwithstanding any copyright notation herein.

847 Acknowledgments

848 Additional information can be given in the template, such as to not include funder information in
849 the acknowledgments section.

850 References

- 851 Adesnik H, Naka A. Cracking the Function of Layers in the Sensory Cortex. *Neuron*. 2018; 100(5):1028–1043.
- 852 Ainsworth M, Lee S, Cunningham MO, Traub RD, Kopell NJ, Whittington MA. Rates and Rhythms:
853 A Synergistic View of Frequency and Temporal Coding in Neuronal Networks. *Neuron*. 2012;
854 75(4):572 – 583. <http://www.sciencedirect.com/science/article/pii/S089662731200709X>, doi:
855 <http://dx.doi.org/10.1016/j.neuron.2012.08.004>.
- 856 Anderson CT, Sheets PL, Kiritani T, Shepherd GMG. Sublayer-specific microcircuits of corticospinal and corti-
857 costriatal neurons in motor cortex. *Nature neuroscience*. 2010 Jun; 13(6):739–44. doi: [10.1038/nn.2538](https://doi.org/10.1038/nn.2538).
- 858 Apicella AJ, Wickersham IR, Seung HS, Shepherd GM. Laminarly orthogonal excitation of fast-spiking and low-
859 threshold-spiking interneurons in mouse motor cortex. *The Journal of Neuroscience*. 2012; 32(20):7021–
860 7033.
- 861 Arle JE, Shils JL. Motor cortex stimulation for pain and movement disorders. *Neurotherapeutics*. 2008 Jan;
862 5(1):37–49. doi: [10.1016/j.nurt.2007.11.004](https://doi.org/10.1016/j.nurt.2007.11.004).
- 863 Ascoli GA, Donohue DE, Halavi M. NeuroMorpho. Org: a central resource for neuronal morphologies. *Journal*
864 *of Neuroscience*. 2007; 27(35):9247–9251.
- 865 Barbas H, García-Cabezas MÁ. Motor cortex layer 4: less is more. *Trends in neurosciences*. 2015; 38(5):259–
866 261.
- 867 Behabadi BF, Polsky A, Jadi M, Schiller J, Mel BW. Location-dependent excitatory synaptic interactions in pyra-
868 midal neuron dendrites. *PLoS Comput Biol*. 2012; 8(7):e1002599.
- 869 Bensmaia SJ, Miller LE. Restoring sensorimotor function through intracortical interfaces: progress and looming
870 challenges. *Nat Rev Neurosci*. 2014 05; 15(5):313–325. <http://dx.doi.org/10.1038/nrn3724>.
- 871 Bopp R, Holler-Rickauer S, Martin KA, Schuhknecht GF. An ultrastructural study of the thalamic input to
872 layer 4 of primary motor and primary somatosensory cortex in the mouse. *Journal of Neuroscience*. 2017;
873 37(9):2435–2448.

- 874 **Boychuk JA**, Farrell JS, Palmer LA, Singleton AC, Pittman QJ, Teskey GC. HCN channels segregate stimulation-
875 evoked movement responses in neocortex and allow for coordinated forelimb movements in rodents. *The
876 Journal of Physiology*. 2017; 595(1):247–263. <https://physoc.onlinelibrary.wiley.com/doi/abs/10.1113/JP273068>,
877 doi: 10.1113/JP273068.
- 878 **Brown SP**, Hestrin S. Intracortical circuits of pyramidal neurons reflect their long-range axonal targets. *Nature*.
879 2009; 457(7233):1133–1136.
- 880 **Bruno RM**, Sakmann B. Cortex is driven by weak but synchronously active thalamocortical synapses. *Science*.
881 2006; 312(5780):1622–1627.
- 882 **Buzsáki G**, Anastassiou CA, Koch C. The origin of extracellular fields and currents—EEG, ECoG, LFP and spikes.
883 *Nature reviews neuroscience*. 2012; 13(6):407.
- 884 **Buzsáki G**, Mizuseki K. The log-dynamic brain: how skewed distributions affect network operations. *Nature
885 Reviews Neuroscience*. 2014; 15(4):264.
- 886 **Carmena JM**. Advances in Neuroprosthetic Learning and Control. *PLoS Biol*. 2013 05; 11(5):e1001561. <http://dx.doi.org/10.1371%2Fjournal.pbio.1001561>, doi: 10.1371/journal.pbio.1001561.
- 888 **Carnevale NT**, Hines ML. *The NEURON book*. Cambridge Univ Pr; 2006.
- 889 **Castro-Alamancos MA**. The motor cortex: a network tuned to 7-14 Hz. *Frontiers in Neural Circuits*. 2013; 7(21).
890 http://www.frontiersin.org/neural_circuits/10.3389/fncir.2013.00021/abstract, doi: 10.3389/fncir.2013.00021.
- 891 **Chadderdon GL**, Mohan A, Suter BA, Neymotin SA, Kerr CC, Francis JT, Shepherd GM, Lytton WW. Motor cortex
892 microcircuit simulation based on brain activity mapping. *Neural computation*. 2014; 26(7):1239–62.
- 893 **Conner J**, Kulczycki M, Tuszyński M. Unique contributions of distinct cholinergic projections to motor cortical
894 plasticity and learning. *Cerebral Cortex*. 2010; 20(11):2739–2748.
- 895 **Constantinople CM**, Bruno RM. Deep cortical layers are activated directly by thalamus. *Science*. 2013;
896 340(6140):1591–1594.
- 897 **Dacre J**, Colligan M, Clarke T, Ammer JJ, Schiemann J, Chamosa-Pino V, Claudi F, Harston JA, Eleftheriou C, Pakan
898 JMP, Huang CC, Hantman AW, Rochefort NL, Duguid I. A cerebellar-thalamocortical pathway drives behavioral
899 context-dependent movement initiation. *Neuron*. 2021; 109(14):2326–2338.e8. <https://www.sciencedirect.com/science/article/pii/S0896627321003561>, doi: <https://doi.org/10.1016/j.neuron.2021.05.016>.
- 901 **Dai K**, Hernando J, Billeh YN, Gratia SL, Planas J, Davison AP, Dura-Bernal S, Gleeson P, Devresse A, Gevaert M,
902 King JG, Van Geit WAH, Povolotsky AV, Muller E, Courcol JD, Arkhipov A. The SONATA Data Format for Efficient
903 Description of Large-Scale Network Models. *bioRxiv*. 2019; <https://www.biorxiv.org/content/early/2019/05/02/625491>, doi: 10.1101/625491.
- 905 **DeFelipe J**, Alonso-Nanclares L, Arellano JI. Microstructure of the neocortex: comparative aspects. *Journal of
906 neurocytology*. 2002; 31(3-5):299–316.
- 907 **Destexhe A**, Bal T, McCormick D, Sejnowski T. Ionic mechanisms underlying synchronized oscillations and
908 propagating waves in a model of ferret thalamic slices. *J Neurophysiol*. 1996; 76:2049–2070.
- 909 **Douglas RJ**, Martin KA, Whitteridge D. A canonical microcircuit for neocortex. *Neural computation*. 1989;
910 1(4):480–488.
- 911 **Dura-Bernal S**, Neymotin SA, Kerr CC, Sivagnanam S, Majumdar A, Francis JT, Lytton WW. Evolutionary al-
912 gorithm optimization of biological learning parameters in a biomimetic neuroprosthesis. *IBM Journal of
913 Research and Development*. 2017 March; 61(2/3):6:1–6:14. doi: 10.1147/JRD.2017.2656758.
- 914 **Dura-Bernal S**, Li K, Neymotin SA, Francis JT, Principe JC, Lytton WW. Restoring behavior via inverse neurocon-
915 troller in a lesioned cortical spiking model driving a virtual arm. *Frontiers in Neuroscience*. 2016; 10(28). <http://www.frontiersin.org/neuroprosthetics/10.3389/fnins.2016.00028/abstract>, doi: 10.3389/fnins.2016.00028.
- 917 **Dura-Bernal S**, Suter BA, Gleeson P, Cantarelli M, Quintana A, Rodriguez F, Kedziora DJ, Chadderdon GL,
918 Kerr CC, Neymotin SA, McDougal RA, Hines M, Shepherd GM, Lytton WW. NetPyNE, a tool for data-driven
919 multiscale modeling of brain circuits. *eLife*. 2019 apr; 8:e44494. <https://doi.org/10.7554/eLife.44494>, doi:
920 10.7554/eLife.44494.
- 921 **Ebbesen CL**, Brecht M. Motor cortex—to act or not to act? *Nature Reviews Neuroscience*. 2017; 18(11):694.

- 922 **Eonomo MN**, Viswanathan S, Tasic B, Bas E, Winnubst J, Menon V, Graybuck LT, Nguyen TN, Smith KA,
923 Yao Z, Wang L, Gerfen CR, Chandrashekar J, Zeng H, Looger LL, Svoboda K. Distinct descending motor
924 cortex pathways and their roles in movement. *Nature*. 2018; 563(7729):79–84. <https://doi.org/10.1038/s41586-018-0642-9>, doi: 10.1038/s41586-018-0642-9.
- 926 **Edelman GM**, Gally JA. Degeneracy and complexity in biological systems. *Proc Nat Acad Sci*. 2001; 98:13763–
927 13768.
- 928 **Estebanez L**, Hoffmann D, Voigt BC, Poulet JFA. Parvalbumin-Expressing GABAergic Neurons in Primary Motor
929 Cortex Signal Reaching. *Cell Reports*. 2018 01/19; 20(2):308–318. <http://dx.doi.org/10.1016/j.celrep.2017.06.044>, doi: 10.1016/j.celrep.2017.06.044.
- 931 **Favero M**, Varghese G, Castro-Alamancos MA. The state of somatosensory cortex during neuromodulation.
932 *Journal of neurophysiology*. 2012; 108(4):1010–1024.
- 933 **Fino E**, Yuste R. Dense inhibitory connectivity in neocortex. *Neuron*. 2011; 69(6):1188–1203.
- 934 **Gal E**, London M, Globerson A, Ramaswamy S, Reimann MW, Muller E, Markram H, Segev I. Rich cell-type-
935 specific network topology in neocortical microcircuitry. *Nat Neurosci*. 2017 07; 20(7):1004–1013. <http://dx.doi.org/10.1038/nn.4576>.
- 937 **George MS**, Abbott L, Siegelbaum SA. HCN hyperpolarization-activated cation channels inhibit EPSPs by inter-
938 actions with M-type K⁺ channels. *Nature neuroscience*. 2009; 12(5):577–584.
- 939 **Gleeson P**, Cantarelli M, Marin B, Quintana A, Earnshaw M, Sadeh S, Piasini E, Birgiolas J, Cannon RC, Cayco-Gajic
940 NA, Crook S, Davison AP, Dura-Bernal S, Ecker A, Hines ML, Idili G, Lanore F, Larson SD, Lytton WW, Majumdar
941 A, et al. Open Source Brain: A Collaborative Resource for Visualizing, Analyzing, Simulating, and Developing
942 Standardized Models of Neurons and Circuits. *Neuron*. 2019 2019/06/11; <https://doi.org/10.1016/j.neuron.2019.05.019>, doi: 10.1016/j.neuron.2019.05.019.
- 944 **Gleeson P**, Crook S, Cannon RC, Hines ML, Billings GO, Farinella M, Morse TM, Davison AP, Ray S, Bhalla US,
945 Barnes SR, Dimitrova YD, Silver RA. NeuroML: A Language for Describing Data Driven Models of Neurons
946 and Networks with a High Degree of Biological Detail. *PLoS Comput Biol*. 2010 06; 6(6):e1000815. <http://dx.doi.org/10.1371%2Fjournal.pcbi.1000815>, doi: 10.1371/journal.pcbi.1000815.
- 948 **Golowasch J**, Goldman M, Abbott L, Marder E. Failure of averaging in the construction of a conductance-based
949 neuron model. *Journal of Neurophysiology*. 2002; 87:1129–1131.
- 950 **Graybiel AM**. Neurotransmitters and neuromodulators in the basal ganglia. *Trends in neurosciences*. 1990;
951 13(7):244–254.
- 952 **Greig LC**, Woodworth MB, Galazo MJ, Padmanabhan H, Macklis JD. Molecular logic of neocortical projection
953 neuron specification, development and diversity. *Nature Reviews Neuroscience*. 2013; 14(11):755.
- 954 **Guo JZ**, Sauerbrei BA, Cohen JD, Mischiati M, Graves AR, Pisanello F, Branson KM, Hantman AW. Disrupting
955 cortico-cerebellar communication impairs dexterity. *eLife*. 2021 jul; 10:e65906. <https://doi.org/10.7554/eLife.65906>, doi: 10.7554/eLife.65906.
- 957 **Harris KD**, Shepherd GM. The neocortical circuit: themes and variations. *Nature Neuroscience*. 2015;
958 18(2):170–181.
- 959 **Hay E**, Hill S, Schürmann F, Markram H, Segev I. Models of Neocortical Layer 5b Pyramidal Cells Capturing
960 a Wide Range of Dendritic and Perisomatic Active Properties. *PLoS Comput Biol*. 2011 07; 7(7):e1002107.
961 <http://dx.doi.org/10.1371%2Fjournal.pcbi.1002107>, doi: 10.1371/journal.pcbi.1002107.
- 962 **Heinze J**, Hepp K, Martin KA. A microcircuit model of the frontal eye fields. *Journal of Neuroscience*. 2007;
963 27(35):9341–9353.
- 964 **Hirata A**, Castro-Alamancos MA. Relief of synaptic depression produces long-term enhancement in thalamo-
965 cortical networks. *Journal of neurophysiology*. 2006; 95(4):2479–2491.
- 966 **Hong G**, Lieber CM. Novel electrode technologies for neural recordings. *Nature Reviews Neuroscience*. 2019;
967 20(6):330–345.
- 968 **Hooks BM**, Mao T, Gutinsky DA, Yamawaki N, Svoboda K, Shepherd GMG. Organization of cortical and
969 thalamic input to pyramidal neurons in mouse motor cortex. *J Neurosci*. 2013 Jan; 33(2):748–760. doi:
970 [10.1523/JNEUROSCI.4338-12.2013](https://doi.org/10.1523/JNEUROSCI.4338-12.2013).

- 971 Hsu NS, Fang HY, David KK, Gnadt JW, Peng GC, Talley EM, Ward JM, Ngai J, Koroshetz WJ. The promise of
972 the BRAIN initiative: NIH strategies for understanding neural circuit function. Current Opinion in Neu-
973 robiology. 2020; 65:162–166. <https://www.sciencedirect.com/science/article/pii/S0959438820301471>, doi:
974 <https://doi.org/10.1016/j.conb.2020.10.008>.
- 975 Hu H, Agmon A. Differential Excitation of Distally versus Proximally Targeting Cortical Interneurons by Unitary
976 Thalamocortical Bursts. Journal of Neuroscience. 2016; 36(26):6906–6916. <http://www.jneurosci.org/content/36/26/6906>, doi: 10.1523/JNEUROSCI.0739-16.2016.
- 978 Isomura Y, Harukuni R, Takekawa T, Aizawa H, Fukai T. Microcircuitry coordination of cortical motor informa-
979 tion in self-initiation of voluntary movements. Nature neuroscience. 2009; 12(12):1586–1593.
- 980 Izhikevich EM, Edelman GM. Large-scale model of mammalian thalamocortical systems. Proceedings of the
981 national academy of sciences. 2008; 105(9):3593–3598.
- 982 Jacob V, Petreanu L, Wright N, Svoboda K, Fox K. Regular spiking and intrinsic bursting pyramidal cells show
983 orthogonal forms of experience-dependent plasticity in layer V of barrel cortex. Neuron. 2012; 73(2):391–
984 404.
- 985 Jahr C, Stevens C. Voltage dependence of NMDA-activated macroscopic conductances predicted by single-
986 channel kinetics. J Neurosci. 1990b; 10(9):3178–3182.
- 987 Kaneko T. Local Connection of Excitatory Neurons in Rat Motor-Associated Cortical Areas. Frontiers in Neu-
988 ral Circuits. 2013; 7(75). http://www.frontiersin.org/neural_circuits/10.3389/fncir.2013.00075/abstract, doi:
989 10.3389/fncir.2013.00075.
- 990 Katzel D, Zemelman BV, Buetfering C, Wolfel M, Miesenbock G. The columnar and laminar organization
991 of inhibitory connections to neocortical excitatory cells. Nat Neurosci. 2011 Jan; 14(1):100–107. doi:
992 10.1038/nn.2687.
- 993 Kiritani T, Wickersham IR, Seung HS, Shepherd GMG. Hierarchical Connectivity and Connection-
994 Specific Dynamics in the Corticospinal-Corticostriatal Microcircuit in Mouse Motor Cortex. The Journal
995 of Neuroscience. 2012; 32(14):4992–5001. <http://www.jneurosci.org/content/32/14/4992.abstract>, doi:
996 10.1523/JNEUROSCI.4759-11.2012.
- 997 Kocaturk M, Gulcur HO, Canbeyli R. Towards building hybrid biological/in silico neural networks for motor
998 neuroprosthetic control. Frontiers in Neurorobotics. 2015; 9(8). <http://www.frontiersin.org/neurorobotics/10.3389/fnbot.2015.00008/abstract>, doi: 10.3389/fnbot.2015.00008.
- 1000 Kole M, Hallermann S, Stuart G. Single Ih channels in pyramidal neuron dendrites: properties, distribution, and
1001 impact on action potential output. Journal of Neuroscience. 2006; 26(6):1677–1687.
- 1002 Konstantoudaki X, Papoutsis A, Chalkiadaki K, Poirazi P, Sidiropoulou K. Modulatory effects of inhibition on
1003 persistent activity in a cortical microcircuit model. Frontiers in Neural Circuits. 2014; 8:7. <http://journal.frontiersin.org/article/10.3389/fncir.2014.00007>, doi: 10.3389/fncir.2014.00007.
- 1005 Kubota Y, Kondo S, Nomura M, Hatada S, Yamaguchi N, Mohamed AA, Karube F, Lübke J, Kawaguchi Y. Func-
1006 tional effects of distinct innervation styles of pyramidal cells by fast spiking cortical interneurons. eLife. 2015
1007 jul; 4:e07919. <https://dx.doi.org/10.7554/eLife.07919>, doi: 10.7554/eLife.07919.
- 1008 Labarrera C, Deitcher Y, Dudai A, Weiner B, Amichai AK, Zylbermann N, London M. Adrenergic Modulation
1009 Regulates the Dendritic Excitability of Layer 5 Pyramidal Neurons In Vivo. Cell reports. 2018; 23(4):1034–
1010 1044.
- 1011 Laudanski J, Torben-Nielsen B, Segev I, Shamma S. Spatially Distributed Dendritic Resonance Selectively Filters
1012 Synaptic Input. PLoS Comput Biol. 2014 08; 10(8):1–10. <http://dx.doi.org/10.1371/journal.pcbi.1003775>,
1013 doi: 10.1371/journal.pcbi.1003775.
- 1014 Lefort S, Tomm C, Floyd Sarria JC, Petersen CCH. The Excitatory Neuronal Network of the C2 Barrel Column in
1015 Mouse Primary Somatosensory Cortex. Neuron. 2009 2015/10/05; 61(2):301–316. <http://dx.doi.org/10.1016/j.neuron.2008.12.020>, doi: 10.1016/j.neuron.2008.12.020.
- 1017 Li K, Dura-Bernal S, Francis J, Lytton W, Principe J. Repairing Lesions via Kernel Adaptive Inverse Control in
1018 a Biomimetic Model of Sensorimotor Cortex. In: *Neural Engineering (NER), 2015 7th International IEEE/EMBS*
1019 Conference Montpellier; 2015. .

- 1020 Li N, Chen TW, Guo ZV, Gerfen CR, Svoboda K. A motor cortex circuit for motor planning and movement. *Nature*.
1021 2015 03; 519(7541):51–56. <http://dx.doi.org/10.1038/nature14178>.
- 1022 Li N, Daie K, Svoboda K, Druckmann S. Robust neuronal dynamics in premotor cortex during motor planning.
1023 *Nature*. 2016 04; 532(7600):459–464. <http://dx.doi.org/10.1038/nature17643>.
- 1024 Lindén H, Hagen E, Leski S, Norheim E, Pettersen K, Einevoll G. LFPy: A tool for biophysical simulation of
1025 extracellular potentials generated by detailed model neurons. *Front Neuroinform*. 2013; 7:41.
- 1026 London M, Häusser M. Dendritic computation. *Annu Rev Neurosci*. 2005; 28:503–532.
- 1027 Luo L, Callaway EM, Svoboda K. Genetic dissection of neural circuits: a decade of progress. *Neuron*. 2018;
1028 98(2):256–281.
- 1029 Lytton WW, Seidenstein A, Dura-Bernal S, Schurmann F, RobertAMcDougal, Hines ML. Simulation neurotech-
1030 nologies for advancing brain research: Parallelizing large networks in NEURON. *Neural Computation*. 2016;
1031 28:2063–2090.
- 1032 Magee JC, Cook EP. Somatic EPSP amplitude is independent of synapse location in hippocampal pyramidal
1033 neurons. *Nature neuroscience*. 2000; 3(9):895–903.
- 1034 Mao T, Kusefoglu D, Hooks BM, Huber D, Petreanu L, Svoboda K. Long-Range Neuronal Circuits Underlying the
1035 Interaction between Sensory and Motor Cortex. *Neuron*. 2011 2016/12/07; 72(1):111–123. <http://dx.doi.org/10.1016/j.neuron.2011.07.029>, doi: 10.1016/j.neuron.2011.07.029.
- 1037 Markram H, Muller E, Ramaswamy S, Reimann M, Abdellah M, Sanchez C, Ailamaki A, Alonso-Nanclares L,
1038 Antille N, Arsever S, Kahou G, Berger T, Bilgili A, Buncic N, Chalimourda A, Chindemi G, Courcol J, Delalondre
1039 F, Delattre V, Druckmann S, et al. Reconstruction and simulation of neocortical microcircuitry. *Cell*. 2015;
1040 163:456–492.
- 1041 Markram H, Muller E, Ramaswamy S, Reimann MW, Abdellah M, Sanchez CA, Ailamaki A, Alonso-Nanclares L,
1042 Antille N, Arsever S, Kahou GAA, Berger TK, Bilgili A, Buncic N, Chalimourda A, Chindemi G, Courcol JD, Delalon-
1043 dre F, Delattre V, Druckmann S, et al. Reconstruction and Simulation of Neocortical Microcircuitry. *Cell*. 2015
1044 2015/10/09; 163(2):456–492. <http://dx.doi.org/10.1016/j.cell.2015.09.029>, doi: 10.1016/j.cell.2015.09.029.
- 1045 McCormick DA. Neurotransmitter actions in the thalamus and cerebral cortex and their role in neuromodula-
1046 tion of thalamocortical activity. *Progress in neurobiology*. 1992; 39(4):337–388.
- 1047 McDougal R, Hines M, Lytton W. Reaction-diffusion in the NEURON simulator. *Frontiers in Neuroinformatics*.
1048 2013; 7:28. <http://journal.frontiersin.org/article/10.3389/fninf.2013.00028>, doi: 10.3389/fninf.2013.00028.
- 1049 Meyer HS, Wimmer VC, Hemberger M, Bruno RM, de Kock CP, Frick A, Sakmann B, Helmstaedter M. Cell type-
1050 specific thalamic innervation in a column of rat vibrissal cortex. *Cerebral Cortex*. 2010; 20(10):2287–2303.
- 1051 Meyer HS, Wimmer VC, Oberlaender M, De Kock CP, Sakmann B, Helmstaedter M. Number and laminar dis-
1052 tribution of neurons in a thalamocortical projection column of rat vibrissal cortex. *Cerebral cortex*. 2010;
1053 20(10):2277–2286.
- 1054 Migliore M, Migliore R. Know Your Current Ih: Interaction with a Shunting Current Explains the Puzzling Effects
1055 of Its Pharmacological or Pathological Modulations. *PLOS ONE*. 2012 05; 7(5):1–8. <https://doi.org/10.1371/journal.pone.0036867>, doi: 10.1371/journal.pone.0036867.
- 1057 Morishima M, Kawaguchi Y. Recurrent connection patterns of corticostriatal pyramidal cells in frontal cortex.
1058 *J Neurosci*. 2006 Apr; 26(16):4394–4405. doi: 10.1523/JNEUROSCI.0252-06.2006.
- 1059 Morishima M, Morita K, Kubota Y, Kawaguchi Y. Highly differentiated projection-specific cortical subnetworks.
1060 *Journal of Neuroscience*. 2011; 31(28):10380–10391.
- 1061 Mott MC, Gordon JA, Koroshetz WJ. The NIH BRAIN Initiative: Advancing neurotechnologies, integrating disci-
1062 plines. *PLOS Biology*. 2018 11; 16(11):1–5. <https://doi.org/10.1371/journal.pbio.3000066>, doi: 10.1371/jour-
1063 nal.pbio.3000066.
- 1064 Muñoz-Castañeda R, Zingg B, Matho KS, Chen X, Wang Q, Foster NN, Li A, Narasimhan A, Hirokawa KE, Huo B,
1065 et al. Cellular anatomy of the mouse primary motor cortex. *Nature*. 2021; 598(7879):159–166.
- 1066 Myme CIO, Sugino K, Turrigiano GG, Nelson SB. The NMDA-to-AMPA Ratio at Synapses Onto Layer 2/3 Pyrami-
1067 dal Neurons Is Conserved Across Prefrontal and Visual Cortices. *Journal of Neurophysiology*. 2003; 90(2):771–
1068 779. <http://jn.physiology.org/content/90/2/771>, doi: 10.1152/jn.00070.2003.

- 1069 Naka A, Adesnik H. Inhibitory circuits in cortical layer 5. *Frontiers in Neural Circuits*. 2016; 10(35). http://www.frontiersin.org/neural_circuits/10.3389/fncir.2016.00035/abstract, doi: 10.3389/fncir.2016.00035.
- 1070
- 1071 Network BICC. A multimodal cell census and atlas of the mammalian primary motor cortex. *Nature*. 2021; 598(7879):86.
- 1072
- 1073 Newton AJH, McDougal RA, Hines ML, Lytton WW. Using NEURON for Reaction-Diffusion Modeling of Extracellular Dynamics. *Frontiers in Neuroinformatics*. 2018; 12:41. <https://www.frontiersin.org/article/10.3389/fninf.2018.00041>, doi: 10.3389/fninf.2018.00041.
- 1074
- 1075
- 1076 Neymotin S, Dura-Bernal S, Lakatos P, Sanger T, Lytton W. Multitarget multiscale simulation for pharmacological treatment of dystonia in motor cortex. *Front Pharmacol*. 2016; 7:157.
- 1077
- 1078 Neymotin S, Suter B, Dura-Bernal S, Shepherd G, Migliore M, Lytton W. Optimizing computer models of corticospinal neurons to replicate in vitro dynamics. *J Neurophysiol*. 2017; 117:148–162.
- 1079
- 1080 Neymotin SA, Dura-Bernal S, Lakatos P, Sanger TD, Lytton W. Multitarget multiscale simulation for pharmacological treatment of dystonia in motor cortex. *Frontiers in Pharmacology*. 2016; 7(157). http://www.frontiersin.org/experimental_pharmacology_and_drug_discovery/10.3389/fphar.2016.00157/abstract, doi: 10.3389/fphar.2016.00157.
- 1081
- 1082
- 1083
- 1084 Neymotin SA, Dura-Bernal S, Moreno H, Lytton WW. Computer modeling for pharmacological treatments for dystonia. *Drug Discovery Today: Disease Models*. 2016; 19:51 – 57. <http://www.sciencedirect.com/science/article/pii/S1740675717300099>, doi: <http://dx.doi.org/10.1016/j.ddmod.2017.02.003>, computational Models of Neurological Disorder.
- 1085
- 1086
- 1087
- 1088 Nishimura Y, Perlmutter SI, Fetz EE. Restoration of upper limb movement via artificial corticospinal and musculospinal connections in a monkey with spinal cord injury. *Frontiers in Neural Circuits*. 2013; 7(57). http://www.frontiersin.org/neural_circuits/10.3389/fncir.2013.00057/abstract, doi: 10.3389/fncir.2013.00057.
- 1089
- 1090
- 1091 O'Donnell J, Zeppenfeld D, McConnell E, Pena S, Nedergaard M. Norepinephrine: a neuromodulator that boosts the function of multiple cell types to optimize CNS performance. *Neurochemical research*. 2012; 37(11):2496–2512.
- 1092
- 1093
- 1094 Oh SW, Harris JA, Ng L, Winslow B, Cain N, Mihalas S, Wang Q, Lau C, Kuan L, Henry AM, et al. A mesoscale connectome of the mouse brain. *Nature*. 2014; 508(7495):207–214.
- 1095
- 1096 Oswald MJ, Tantirigama ML, Sonntag I, Hughes SM, Empson RM. Diversity of Layer 5 Projection Neurons in the Mouse Motor Cortex. *Frontiers in Cellular Neuroscience*. 2013; 7(174). http://www.frontiersin.org/cellular_neuroscience/10.3389/fncel.2013.00174/abstract, doi: 10.3389/fncel.2013.00174.
- 1097
- 1098
- 1099 Papale AE, Hooks BM. Circuit changes in motor cortex during motor skill learning. *Neuroscience*. 2017; .
- 1100 Parasuram H, Nair B, D'Angelo E, Hines M, Naldi G, Diwakar S. Computational Modeling of Single Neuron Extracellular Electric Potentials and Network Local Field Potentials using LFPsim. *Frontiers in Computational Neuroscience*. 2016; 10:65. <https://www.frontiersin.org/article/10.3389/fncom.2016.00065>, doi: 10.3389/fncom.2016.00065.
- 1101
- 1102
- 1103
- 1104 Peters AJ, Lee J, Hedrick NG, O'Neil K, Komiyama T. Reorganization of corticospinal output during motor learning. *Nature neuroscience*. 2017; .
- 1105
- 1106 Petreanu L, Mao T, Sternson SM, Svoboda K. The subcellular organization of neocortical excitatory connections. *Nature*. 2009; 457(7233):1142–1145.
- 1107
- 1108 Poirazi P, Papoutsis A. Illuminating dendritic function with computational models. *Nature Reviews Neuroscience*. 2020; 21(6):303–321.
- 1109
- 1110 Potjans TC, Diesmann M. The Cell-Type Specific Cortical Microcircuit: Relating Structure and Activity in a Full-Scale Spiking Network Model. *Cerebral Cortex*. 2014; 24(3):785–806. <http://cercor.oxfordjournals.org/content/24/3/785.abstract>, doi: 10.1093/cercor/bhs358.
- 1111
- 1112
- 1113 Prinz A, Marder E. Using a database of 20 million model networks to study a pacemaker circuit. *Soc Neurosci Abstracts*. 2003; 605.3.
- 1114
- 1115 Rees CL, Moradi K, Ascoli GA. Weighing the Evidence in Peters' Rule: Does Neuronal Morphology Predict Connectivity? *Trends Neurosci*. 2017; 40:63–71.
- 1116

- 1117 **Rubino D**, Robbins KA, Hatsopoulos NG. Propagating waves mediate information transfer in the motor cortex.
1118 Nat Neurosci. 2006 Dec; 9(12):1549–1557. doi: 10.1038/nn1802.
- 1119 **Rumsey CC**, Abbott LF. Synaptic democracy in active dendrites. Journal of Neurophysiology. 2006; 96(5):2307–
1120 2318.
- 1121 **Sanchez J**, Lytton W, Carmena J, Principe J, Fortes J, Barbour R, Francis J. Dynamically repairing and replacing
1122 neural networks: using hybrid computational and biological tools. IEEE Pulse. 2012 Jan; 3(1):57–59. doi:
1123 [10.1109/MPUL.2011.2175640](https://doi.org/10.1109/MPUL.2011.2175640).
- 1124 **Schieber MH**. Dissociating motor cortex from the motor. The Journal of physiology. 2011; 589(23):5613–5624.
- 1125 **Schiemann J**, Puggioni P, Dacre J, Pelko M, Domanski A, van Rossum MCW, Duguid I. Cellular Mechanisms
1126 Underlying Behavioral State-Dependent Bidirectional Modulation of Motor Cortex Output. Cell Reports.
1127 2015; 11(8):1319 – 1330. <http://www.sciencedirect.com/science/article/pii/S22112471500443X>, doi:
1128 <https://doi.org/10.1016/j.celrep.2015.04.042>.
- 1129 **Schmidt M**, Bakker R, Shen K, Bezgin G, Diesmann M, van Albada SJ. A multi-scale layer-resolved spiking network
1130 model of resting-state dynamics in macaque visual cortical areas. PLOS Computational Biology. 2018 10;
1131 14(10):1–38. <https://doi.org/10.1371/journal.pcbi.1006359>, doi: 10.1371/journal.pcbi.1006359.
- 1132 **Schüz A**, Palm G. Density of neurons and synapses in the cerebral cortex of the mouse. Journal of Comparative
1133 Neurology. 1989; 286(4):442–455.
- 1134 **Sheets PL**, Suter BA, Kiritani T, Chan CS, Surmeier DJ, Shepherd GM. Corticospinal-specific HCN expression in
1135 mouse motor cortex: Ih-dependent synaptic integration as a candidate microcircuit mechanism involved in
1136 motor control. Journal of neurophysiology. 2011; 106(5):2216–2231.
- 1137 **Shenoy KV**, Carmena JM. Combining Decoder Design and Neural Adaptation in Brain-Machine Interfaces. Neu-
1138рон. 2014; 84(4):665–680.
- 1139 **Shepherd GM**. Corticostriatal connectivity and its role in disease. Nature Reviews Neuroscience. 2013; .
- 1140 **Shepherd GM**. Intracortical cartography in an agranular area. Frontiers in neuroscience. 2009; 3:30.
- 1141 **Sohal VS**, Zhang F, Yizhar O, Deisseroth K. Parvalbumin neurons and gamma rhythms enhance cortical circuit
1142 performance. Nature. 2009; 459(7247):698.
- 1143 **Spruston N**. Pyramidal neurons: dendritic structure and synaptic integration. Nature Reviews Neuroscience. 2008;
1144 9(3):206–221.
- 1145 **Stepanyants A**, Martinez LM, Ferecskó AS, Kisvárdy ZF. The fractions of short-and long-range connections in
1146 the visual cortex. Proceedings of the National Academy of Sciences. 2009; 106(9):3555–3560.
- 1147 **Suter BA**, Migliore M, Shepherd GM. Intrinsic electrophysiology of mouse corticospinal neurons: a class-specific
1148 triad of spike-related properties. Cerebral Cortex. 2013; 23(8):1965–1977.
- 1149 **Suter BA**, Shepherd GM. Reciprocal Interareal Connections to Corticospinal Neurons in Mouse M1 and S2. The
1150 Journal of Neuroscience. 2015; 35(7):2959–2974.
- 1151 **Tripathy SJ**, Burton SD, Geramita M, Gerkin RC, Urban NN. Brain-wide analysis of electrophysiological diversity
1152 yields novel categorization of mammalian neuron types. Journal of Neurophysiology. 2015; 113(10):3474–
1153 3489. <http://jn.physiology.org/content/113/10/3474>, doi: 10.1152/jn.00237.2015.
- 1154 **Tsai PS**, Kaufhold JP, Blinder P, Friedman B, Drew PJ, Karten HJ, Lyden PD, Kleinfeld D. Correlations of neuronal
1155 and microvascular densities in murine cortex revealed by direct counting and colocalization of nuclei and
1156 vessels. The Journal of Neuroscience. 2009; 29(46):14553–14570.
- 1157 **Tsubo Y**, Isomura Y, Fukai T. Neural dynamics and information representation in microcircuits of motor cortex.
1158 Frontiers in Neural Circuits. 2013; 7:85. <http://journal.frontiersin.org/article/10.3389/fncir.2013.00085>, doi:
1159 [10.3389/fncir.2013.00085](https://doi.org/10.3389/fncir.2013.00085).
- 1160 **Wall NR**, De La Parra M, Sorokin JM, Taniguchi H, Huang ZJ, Callaway EM. Brain-Wide Maps of Synaptic Input
1161 to Cortical Interneurons. The Journal of Neuroscience. 2016; 36(14):4000–4009.
- 1162 **Wang Y**, Hutchings F, Kaiser M. Computational modeling of neurostimulation in brain diseases. Progress in
1163 brain research. 2015; 222:191–228.

- 1164 **Wang Z**, McCormick DA. Control of firing mode of corticotectal and corticopontine layer V burst-generating
1165 neurons by norepinephrine, acetylcholine, and 1S, 3R-ACPD. *Journal of Neuroscience*. 1993; 13(5):2199–
1166 2216.
- 1167 **Weiler N**, Wood L, Yu J, Solla SA, Shepherd GMG. Top-down laminar organization of the excitatory network in
1168 motor cortex. *Nat Neurosci*. 2008 Mar; 11(3):360–366. doi: 10.1038/nn2049.
- 1169 **Winnubst J**, Bas E, Ferreira TA, Wu Z, Economo MN, Edson P, Arthur BJ, Bruns C, Rokicki K, Schauder D, Olbris
1170 DJ, Murphy SD, Ackerman DG, Arshadi C, Baldwin P, Blake R, Elsayed A, Hasan M, Ramirez D, Dos Santos B,
1171 et al. Reconstruction of 1,000 Projection Neurons Reveals New Cell Types and Organization of Long-Range
1172 Connectivity in the Mouse Brain. *Cell*. 2019; 179(1):268–281.e13. <https://www.sciencedirect.com/science/article/pii/S0092867419308426>, doi: <https://doi.org/10.1016/j.cell.2019.07.042>.
- 1174 **Yamashita T**, Pala A, Pedrido L, Kremer Y, Welker E, Petersen CC. Membrane potential dynamics of neocortical
1175 projection neurons driving target-specific signals. *Neuron*. 2013; 80(6):1477–1490.
- 1176 **Yamawaki N**, Borges K, Suter BA, Harris KD, Shepherd GM. A genuine layer 4 in motor cortex with prototypical
1177 synaptic circuit connectivity. *Elife*. 2015; 3:e05422.
- 1178 **Yamawaki N**, Shepherd GMG. Synaptic circuit organization of motor corticothalamic neurons. *The Journal of
1179 Neuroscience*. 2015; 35(5):2293–2307.
- 1180 **Yamawaki N**, Tapies MGR, Stults A, Smith GA, Shepherd GM. Circuit organization of the excitatory sensorimotor
1181 loop through hand/forelimb S1 and M1. *Elife*. 2021; 10:e66836.
- 1182 **Yu J**, Anderson CT, Kiritani T, Sheets PL, Wokosin D, Wood L, Shepherd GM. Local-circuit phenotypes of layer 5
1183 neurons in motor-frontal cortex of YFP-H mice. *Frontiers in neural circuits*. 2008; 2:6.
- 1184 **Zagha E**, Ge X, McCormick DA. Competing neural ensembles in motor cortex gate goal-directed motor output.
1185 *Neuron*. 2015; 88(3):565–577.
- 1186 **Zareian B**, Zhang Z, Zagha E. Cortical Localization of the Sensory-Motor Transformation in a Whisker Detection
1187 Task in Mice. *Eneuro*. 2021; 8(1).
- 1188 **Zeng H**, Sanes JR. Neuronal cell-type classification: challenges, opportunities and the path forward. *Nature
1189 Reviews Neuroscience*. 2017; 18(9):530.
- 1190 **Zhang M**, Eichhorn SW, Zingg B, Yao Z, Cotter K, Zeng H, Dong H, Zhuang X. Spatially resolved cell atlas of the
1191 mouse primary motor cortex by MERFISH. *Nature*. 2021; 598(7879):137–143.
- 1192 **Zhang S**, Xu M, Chang WC, Ma C, Do JPH, Jeong D, Lei T, Fan JL, Dan Y. Organization of long-range inputs and
1193 outputs of frontal cortex for top-down control. *Nature Neuroscience*. 2016; .